ROYAL INSTITUTE
OF TECHNOLOGY

Liquid-Jet-Target Microfocus X-Ray Sources:

Electron Guns, Optics and Phase-Contrast Imaging

Tomi Tuohimaa

Doctoral Thesis

Department of Applied Physics

Royal Institute of Technology

Stockholm, Sweden 2008

TRITA-FYS 2008:21

ISSN 0280-316X

ISRN KTH/FYS/--08:21--SE

ISBN 978-91-7415-004-9

Akademisk avhandling som med tillstånd av Kungliga Tekniska Högskolan framlägges till offentlig granskning för avläggande av teknologie doktorsexamen fredagen den 13 juni 2008 klockan 14.00 i Sal FD5, Roslagstullsbacken 21, KTH/Albanova, Stockholm.

Tryck: Universitetsservice US AB

Abstract

This Thesis describes the development of an electron-impact microfocus x-ray source and its application for phase-contrast imaging. The source is based on a novel, liquid-jet target concept. Stable and continuous operation can be achieved at substantially higher electron-beam power densities than conventional solid target based systems. The maximum x-ray brightness can potentially be increased by a factor of 10-1000, which would provide significantly improved performance in applications such as imaging.

In order to reach the high x-ray brightness, comparable performance from the electron gun is needed. A LaB_6-cathode-based electron gun is analyzed in terms of achievable e-beam brightness and beam quality and is found capable to deliver power densities in the 10-100 MW/mm² range using optimized electro-optics.

A proof-of-principle microfocus source has been developed. Experiments show that the liquid-metal-jet target can be operated at more than an order of magnitude higher e-beam power densities than modern solid-metal targets. This brightness enhancement has been utilized to acquire in-line phase-contrast images of weakly absorbing objects. The source potentially enables the application of high-resolution phase-contrast x-ray imaging with short exposure times in clinics and laboratories.

Different liquid-jet-target materials have been tested. The Sn-jet (K_α=25.3 keV) could be suitable for mammography, whereas the Ga-jet (K_α=9.2 keV) may be utilized for x-ray diffraction studies. In addition, a non-metallic methanol jet has been the demonstrated in stable x-ray operation. All materials and compounds found in liquid form can, thus, potentially be used for electron-impact liquid-jet-target x-ray generation.

Scaling to higher e-beam power density and x-ray brightness levels is discussed and is determined to be feasible. Potential difficulties, such as debris emission and instabilities of the x-ray emission spot, are investigated in some detail. Larger and/or faster jets could overcome the present limitations because of their inherently higher heat load capacities. Dynamic-similarity experiments show that liquid jets can in principle be operated in a stable manner at much higher speeds than previously shown.

List of Papers

This Thesis is based on the following Papers:

Paper 1. T. T. Tuohimaa, M. Otendal, and H. M. Hertz, *High-Intensity Electron Beam for Liquid-Metal-Jet-Anode Hard X-Ray Generation*, Proc. SPIE **5918**, 225 (2005).

Paper 2. M. Otendal, O. Hemberg, T. T. Tuohimaa, H. M. Hertz, *Microscopic High-Speed Liquid-Metal Jets in Vacuum*, Exp. Fluids **39**, 799 (2005).

Paper 3. M. Otendal, T. Tuohimaa and H.M. Hertz, *Stability and Debris in High-Brightness Liquid-Metal-Jet-Anode Microfocus X-Ray Sources* J. Appl. Phys. **101,** 026102 (2007).

Paper 4. T. Tuohimaa, M. Otendal, and H. M. Hertz, *Phase-Contrast X-Ray Imaging with a Liquid-Metal-Jet-Anode Microfocus Source*, Appl. Phys. Lett. **91**, 074104 (2007).

Paper 5. M. Otendal, T. Tuohimaa, U. Vogt, and H. M. Hertz, *A 9-keV Electron-Impact Liquid-Gallium-Jet X-Ray Source*, Rev. Sci. Instr. **79**, 016102 (2008).

Paper 6. T. Tuohimaa, J. Ewald, M. Schlie, J. M. Fernandez-Varea, , H. M. Hertz and U. Vogt, *A Microfocus X-Ray Source using a Methanol-Jet-Anode*, submitted to Appl. Phys. Lett.

Other Publications

The following Papers, contributed to by the author, are related to the work in this thesis, but are not included in it.

M. Otendal, T. T. Tuohimaa, O. Hemberg, and H. M. Hertz, *Status of the Liquid-Metal-Jet-Anode Electron-Impact X-Ray Source*, Proc. SPIE **5537**, 57 (2004).

U. Vogt, M. Lindblom, P. A. C Jansson, T. T. Tuohimaa, A. Holmberg, H. M. Hertz, M. Wieland and T. Wilhein, *Single-Optical-Element Soft X-Ray Interferometry with a Laser- Plasma Source*, Opt. Lett. **30,** 2167 (2005).

M. Lindén, T. Tuohimaa, A. B. Jonsson, M. Wallin, *Force Generation in Small Ensembles of Brownian Motors,* Phys. Rev. E , Stat. Nonlin. Soft Matter Phys. **74**, 021908 (2006).

M. Lindblom, T. Tuohimaa, A. Holmberg, T. Wilhein, H. M. Hertz, and U. Vogt, *High-Resolution Differential-Interference-Contrast X-Ray Zone Plates: Design and Fabrication*, Spectrochimica Acta **B62**, 539 (2007).

Contents

Chapter 1

Introduction

X-rays are used for a wide variety of purposes in industry, medicine and research. The penetrating nature of x-rays enables investigations of internal structures of normally opaque objects and consequently, x-ray imaging is also among the most important tools in medical diagnostics. Non-destructive testing using x-rays is also a common inspection method [1] where the demands for resolution and throughput are increasing, particularly in the semiconductor industry. In addition, the short wavelength enables structure determination of materials on an atomic scale via diffraction experiments. [2]

A good figure of merit for any radiating source is its brightness, customarily expressed in radiated power per unit source area and unit solid angle. However, brightness is at best conserved in a perfect optical system. [3] Thus, any improvement must stem from the source, motivating the construction of dedicated synchrotron facilities, built specifically for producing high-brightness radiation. [4] Their high brightness enables research, such as phase-contrast imaging, which normally is too time consuming or downright impossible with conventional x-ray sources. In general, many applications are source limited, thus any increase in compact x-ray source brightness is beneficial and can potentially enable research, today primarily conducted at synchrotrons, to be carried out in a lab environment.

Compact electron-impact x-ray tubes, which are used for the majority of industrial and medical radiography applications today, are fundamentally limited in x-ray brightness due to thermal limitations in the target. This Thesis describes an electron impact x-ray source based on a novel, liquid-jet-based target concept. Stable and continuous operation can be achieved at substantially higher electron beam power densities than conventional solid targets. The maximum x-ray brightness can potentially be increased by a factor of 10-1000, which would give significantly improved x-ray imaging properties. [5,6]

The Thesis begins with a brief introduction to the operational principles of electron-impact x-ray tubes, in particular liquid-jet based, in Chapter 2. In Chapter

3, the background of the design of the high-brightness electron beam which is necessary to fully utilize the enhanced heat load capacity of the liquid-jet-target. Chapter 4 provides an overview of the thermal and x-ray emission properties of electron-impact targets, particularly liquid-jets. The present performance of the liquid-jet-target x-ray system is then investigated in detail in Chapter 5. Finally, Chapter 6 is devoted to an application example, namely in-line phase-contrast x-ray imaging, an imaging technique where improved x-ray brightness has a large impact on the performance.

Chapter 2

Electron-Impact X-Ray Sources

The vast majority of x-ray sources are based on electron-impact on solid targets. The x-ray brightness generated by an electron impact x-ray tube is limited by a number of factors: (i) the maximum brightness of the electron source which is consistent with a useful cathode lifetime; (ii) the properties of the electron-optical system; (iii) the highest power density the target can sustain without performance degradations or damage and (iv) the efficiency of the x-ray generation in the target material including any self absorption effects.

2.1 Principles of Operation

The x-ray tube in its most basic form consists of a cathode and grounded anode, cf. Fig 2.1a. An electron beam strikes the anode and x-rays are generated via bremsstrahlung and ionization (cf. Appendix) of the anode material. The vast majority of all x-ray tubes are constructed in this manner. Often improved control of the e-beam profile impinging on the target is needed. For this purpose the arrangement of Fig. 2.1b is used, where a hole is made in the anode plate. This causes the electron beam "miss" the grounded anode and thus continue into a region customarily denoted as the optical column, where electron optics can be used for beam manipulation and focusing.

2.2 Electron Beam Power Density vs. X-Ray Brightness

An important figure-of-merit for x-ray systems is the brightness of the source, which should be as high as possible to be able to achieve a higher spatial resolution and/or a short exposure time. However, the x-ray brightness is fundamentally limited by the maximum possible heat dissipation of the x-ray target. As an electron beam strikes a metallic target, the energy is converted into heat and x-rays. The conversion efficiency into x-rays is very poor, typically 0.5-1%, whereas the remaining energy heats the target.

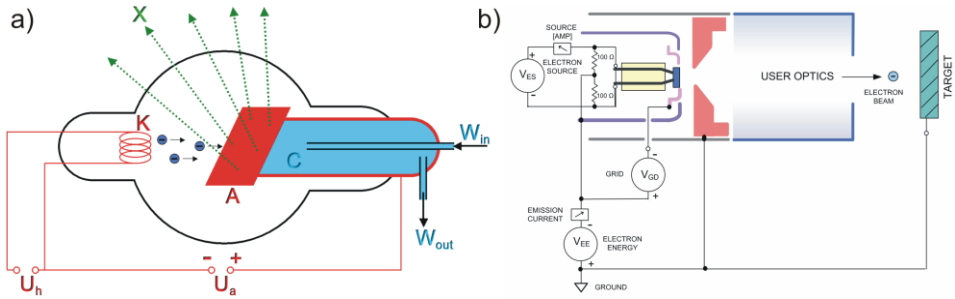

Figure 2.1. a) A stationary target x-ray tube. U_a is the beam accelerating voltage applied between cathode and anode. U_h is the cathode heater voltage which floats at high voltage. The grounded anode also acts as the x-ray generating target. In this case the anode is cooled with circulating water. Adapted from [7] b) An electron gun for high brightness beam formation. The electrical circuit is similar to that depicted in Fig. 2.1 but with a grid voltage, V_{GD} added. This can be used to pulse the beam and/or manipulate the electric fields at the cathode. Adapted from [8]

Thus, in conventional solid-target tubes, exceeding a critical material-dependent power density will result in a damaged target. Therefore, an increased x-ray flux requires larger target area, which results in lower spatial resolution in imaging applications. As a consequence, for obtaining high flux *and* good spatial resolution, one has to increase the brightness, β_γ of the x-ray tube which is measured as x-ray power per source area and spatial angle or [photons/(second·μm²·sr)]. The x-ray brightness is proportional to the e-beam power density

$$\beta_\gamma \propto \frac{P_e}{A}, \tag{2.1}$$

where P_e and A are the e-beam power and focus size, respectively. Thus, any gains in x-ray source brightness, where the e-beam target stability and structural integrity has to be maintained, have to be achieved by improving the thermal conditions and/or the heat load capacity of the target.

The x-ray brightness of x-ray tubes has improved over the years. The most notable performance increases, in terms of target heat load capacity, were due to the introduction of the line focus concept in the 20's and the rotating-anode in the 30's, cf. Sect. 4.2. Since the discovery of X-rays in 1895, the applicable e-beam power density has increased by about six orders of magnitude due to engineering efforts and material improvements and Table 2.1 shows the historical development of the e-beam load capacity and power of compact electron-impact x-ray sources.

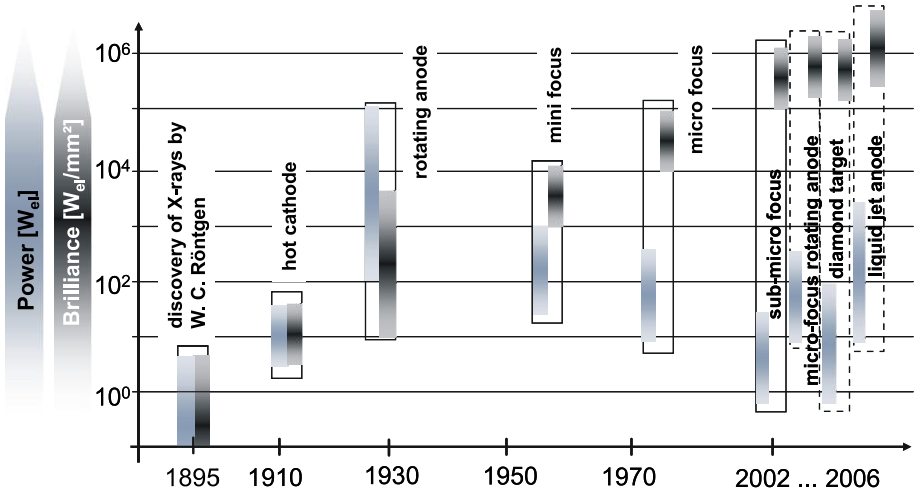

Table 2.1. Historical timeline of x-ray tube performance. Some of the sources shown with a dashed box are under development and are not yet available commercially. Adapted from [1]

2.3 Liquid-Jet-Target X-Ray Sources

As already noted, the limiting factor of conventional electron-impact x-ray tube performance is the electron-beam power-load capacity of the anode. [9] Despite the efforts of further refinement of these x-ray sources it seems unlikely that any significant progress will be made with the use of solid metal anodes. [10]

This has led to research on different types of liquid metal anodes, such as a stationary liquid metal bath [11], a flow of liquid metal across a surface [12], and streaming of liquid metal behind a thin window. [13,14] The major drawback of these sources is the low flow speed which limits the attainable heat load capacity, therefore making them less attractive for many purposes. However, that obstacle can be overcome by using a liquid-metal-jet. The maximum allowed continuous electron-beam power density on the anode could be increased two to three orders of magnitude. In short, this is due to:

- The attainable speed of a liquid-jet is at least an order of magnitude higher than the speed of a rotating anode, see Paper 2 for details.

- A liquid-jet target is regenerative and could therefore be heated to the evaporation point, and possibly also into vaporization, cf. Paper 3 and 6 for a more elaborate discussion on this topic.

- Due to the regenerative nature of the liquid-jet target the maximum source brightness may also be attained in continuous operation, which is not the case for rotating anode sources.

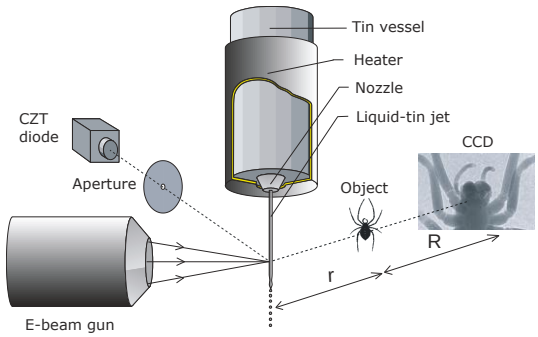

Figure 2.2. The experimental arrangement. An x-ray source is generated by electron impact on a fast moving liquid-jet. From Paper 5.

Figure 2.2 depicts the experimental arrangement used in Papers 1 and 3-6. The gas driven jet is injected into a vacuum tank which is also connected to the electron gun. The high-brightness electron beam is focused using a magnetic lens. By crossing the liquid jet and e-beam focus, a high-brightness x-ray source is created in the interaction point. A number of diagnostic instruments are used for characterization of the system. The breakup behavior of the jet, the x-ray source size and stability, the spectral distribution of the generated x-ray photons, and the source intensity can all be monitored during an experiment. For more detailed information about the experimental arrangement and its present performance, see Papers 1, 3-6 and Chapter 5.

Chapter 3

Basic Electron Physics and Optics

The liquid-jet-target x-ray source consists of two critical components: A high brightness electron gun and the jet anode. In this chapter we discuss the background and brightness limitations of the electron gun and the electron optics used for focusing. Since the research field of electron physics and optics is extremely large and active, we restrict most of the discussions to the thermionic electron sources and focusing systems customarily used for microfocus x-ray generation.

The interested reader can find a more general and detailed background to the topics discussed in this chapter in Refs 15-19 (basic accelerator physics), Refs 20-26 (charged particle optics) and Refs 27 and 28 (numerical methods).

3.1 The Electron Gun

The main task of an electron gun in electron-impact x-ray generation is simple to formulate: to form an intense, high-power-density focus. Figure 3.1 depicts the electron gun used for that purpose in Papers 1 and 3-6. The gun consists of two basic parts, the acceleration gap in a diode configuration, with a cathode at negative high voltage and with the anode grounded and the optical column, used for manipulating and focusing the accelerated beam. In our case we use magnetic fields as optical elements. The maximum power density of the focused beam is highly dependent on the beam brightness that can be produced at the electron source and the focusing capability of the optical column. As we will see later in Sect. 3.6.1 and Chapter 5, there are fundamental limitations to the achievable power density associated with single lens systems such as the one depicted in Fig. 3.1.

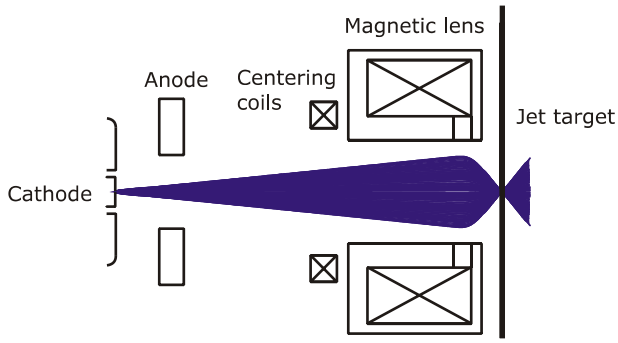

Figure 3.1. The electron gun with its optical column.

3.2 Electron Beam Sources

The type of cathode that can be used in an electron gun for x-ray generation via electron impact is largely determined by two basic parameters dictated by practical constraints: the vacuum conditions in the gun and the amount of beam current needed to create an observable signal in the application.

The different electron emission mechanisms can be divided into three categories:

i. *Thermionic emission*, described by the Richardson-Dushman equation, which together with the Schottky equation describes pure thermal and field-enhanced emission. [29]
ii. *Thermal-field emission*, for cathodes operating in the extended Schottky regime. [30]
iii. *Cold field emission*, where the emission mechanism is described by the Fowler-Nordheim equation. [31]

For general purpose x-ray generation devices the thermal-field and cold-field emission cathodes are generally not practical due to their intrinsically low beam currents and the need for ultra-high-vacuum conditions for stable operation. However, field effects are still important to understand in order to maximize the brightness from thermionic cathodes since they can be operated in the grey zone between field and thermionic emission, also known as the Schottky enhanced emission regime.

3.2.1 Thermionic Cathodes

Thermionic cathodes can be made from wide variety of materials: In fact, all metals and semi-conductors can be made to emit electrons if heated to a high enough temperature. [29] Depending on the application different properties such as vacuum requirements, operation temperature, surface roughness, porosity, and cathode lifetime are decisive in the exact choice of cathode. [32] For high-brightness-electron beam generation, a commonly used thermionic emitter is the single crystal LaB_6 or CeB_6 cathode. A combination of modest vacuum requirements, long lifetime, excellent surface flatness and high emission current capabilities has made it suitable in a wide variety of systems, such as electron microscopes (SEM, TEM), e-beam lithography columns [33], micro focus x-ray tubes [34] and free electron laser injectors [35].

Figure 3.2 shows a custom-made, high performance LaB_6 crystal based cathode with a guard ring of carbon used to enhance the beam quality. [36] The gun used in Papers 1 and 5-6 had a guard ring cathode mounted. The accelerating field is homogeneous over the emitting surface and very bright beams can be achieved due to enhanced field emission. [37-41] Another advantage of using a guard ring is the elimination of the control grid, customarily used to control the size of the emission surface and beam divergence, see Fig. 3.3. The grid distorts the electric field, gives rise to stronger space charge forces and lowers the maximum achievable brightness.[39]

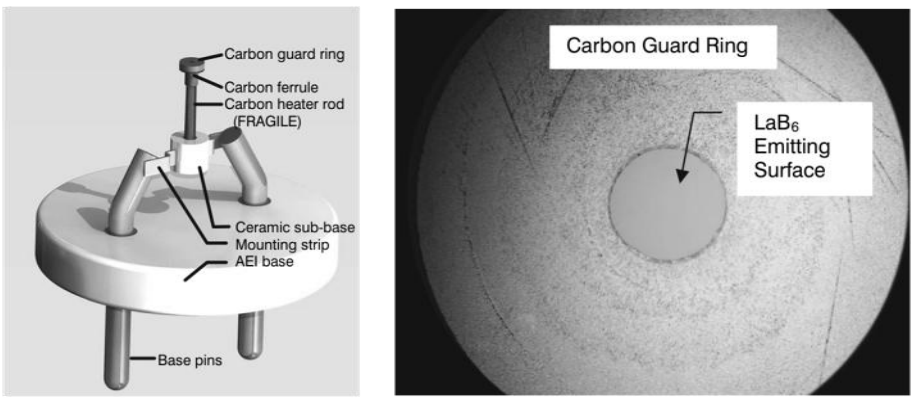

Figure 3.2. Left: A custom-made guard ring cathode with its mount. Right: the emitter surface as seen from above. Adapted from [8].

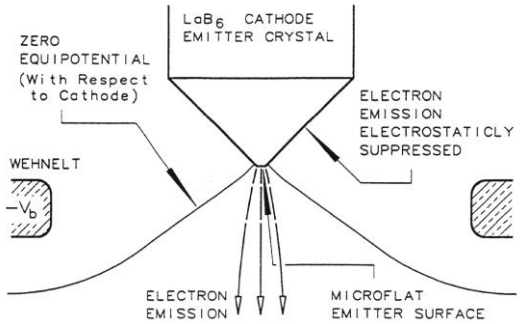

Figure 3.3. A conventional cathode arrangement using a conical cathode with a microflat emitter surface. The electron emission from the conical surface is suppressed with an electrical field from a biased electrode. Adapted from [42].

3.2.2 Thermionic Emission

Thermionic electron emission can be analyzed using a modified Richardson-Dushman equation. [43] Richardson received a Nobel Prize in 1928 "for his work on the thermionic phenomenon and especially for the discovery of the law named after him" and the equation can be written as

$$\rho_c = AT^2 \exp\left[-\frac{e(\Phi_w - \Phi_{qt})}{k_B T}\right], \tag{3.1}$$

where A is material constant, T is the cathode temperature, Φ_w is work function of the material and. Φ_{qt} is a correction factor for quantum tunneling [44], expressed as

$$\Phi_{qt}[\text{eV}] = 0.012\sqrt{E_k[\text{kV/cm}]}, \tag{3.2}$$

where E_k is the electric field strength at the emitter surface. The correction factor Φ_{qt} is highly dependent on the geometry and the electrical fields at the cathode. If properly utilized it can aid in generating current densities substantially higher than what is predicted from the standard Richardson-Dushman equation. [45]

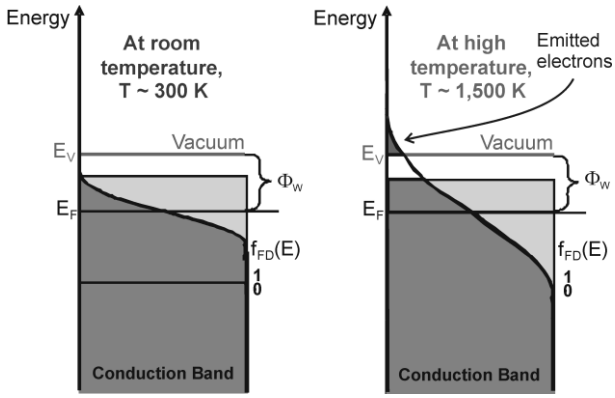

Figure 3.4. Thermionic electron emission. The tail of the Fermi-Dirac distribution, f_{FD}, extends over the vacuum level at elevated temperatures. Adapted from [46]

Electron Source Performance Comparison				
Emitter type	Thermionic	Thermionic	Schottky FE	Cold FE
Cathode material	W	LaB_6	ZrO/W (100)	W (310)
Operating temperature [K]	2800	1900	1800	300
Cathode radius [µm]	Min. 60	Min. 10	≤ 1	≤ 0.1
Emission current density [A/cm^2]	3	30	5300	17000
Total emission current [µA]	≥ 200	≥ 80	200	5
Normalized brightness [A/cm^2·sr·kV].	10^4	10^5	10^7	≥ 10^7
Energy spread at cathode [eV]	0.59	0.40	0.31	0.26
Operating vacuum [mbar]	≤ 10^{-6}	≤ 10^{-7}	≤ 10^{-9}	≤ 10^{-10}
Cathode lifetime [h]	200	1000	2000	2000

Table 3.1. Performance comparison between two thermionic and two field emission cathodes. Adapted from [47].

Figure 3.4 illustrates the physical background to the thermionic emission described by Eq. (3.1). Free electrons from the conduction band are thermally excited by heating and can, thus, leave the material if the temperature is high enough. In the right conditions a cloud of electrons is formed at the material surface. By applying an accelerating field, a beam can be formed. A comparison of the most common electron sources used for micro and nano sized focusing can be found in Table 3.1. Since thermionic cathodes are used in wide range of applications, while field emission cathodes are more commonly found in an electron microscope, the comparison is made assuming that the cathode would be used in a microscopy

column. Some of the parameters, especially for the thermionic sources, might be orders of magnitude different if used in a different application. It can be noted that for x-ray generation with micron-sized electron beam probes, thermionic cathodes are almost exclusively used and the beam current and the cathode radius is often much larger than what is displayed in Table 3.1. Although field emission cathodes are much brighter than the thermionic, the small emission currents and ultra-high vacuum requirements make them impractical to use as electron beam sources for general x-ray generation.

3.3 Electron Acceleration

In order to form a well defined beam of electrons, the electrons have to be accelerated. This is conventionally achieved by setting the cathode at constant negative electrical potential. The maximum, practically achievable beam energy using DC acceleration is ~0.5-1 MeV, already a formidable engineering task. This limit is given by high voltage breakdown, i.e., arcing. This is partially due to the residual gas molecules present in any vacuum system that are ionized and, thus, create a path for a short circuit. In order to reach MeV or GeV electron energies, more advanced acceleration techniques such as radio frequency (RF) cavities are used. [48] Conventional radiography x-ray tubes are usually limited to ~160 kV, but higher acceleration voltages can be found in non-destructive inspection (NDT) x-ray tubes.

3.4 Electron Beam Brightness

The theoretical limitations to the electron beam brightness using a thermionic cathode can be derived from fundamental physical principles. [49,50] Electrons emitted from a hot surface have a Maxwellian energy distribution (the tail of Fermi-Dirac distribution, cf. Fig. 3.4) with a most probable energy of $k_B T$, where k_B is the Boltzmann constant and T is the cathode temperature. Electrons emitted into a field-free space travel out in a Lambertian distribution following the cosine law. These two effects combined give the electrons a transverse velocity component that can never be focused out. In order to create an electron beam, the thermal electrons are accelerated using an applied electrostatic field which increases the electrons velocity component parallel to that field. This acceleration reduces the semi-angle of divergence from π to the ratio of the parallel and radial velocities. If the electrons are accelerated through a potential of V_0, the new velocity will be $(2eV_0/m)^{1/2}$ and hence the new semi-angle will be $(k_B T/eV)^{1/2}$ giving a solid angle

of $\pi k_B T/eV$, assuming that all the electrons have the most probable thermal energy, $k_B T$.

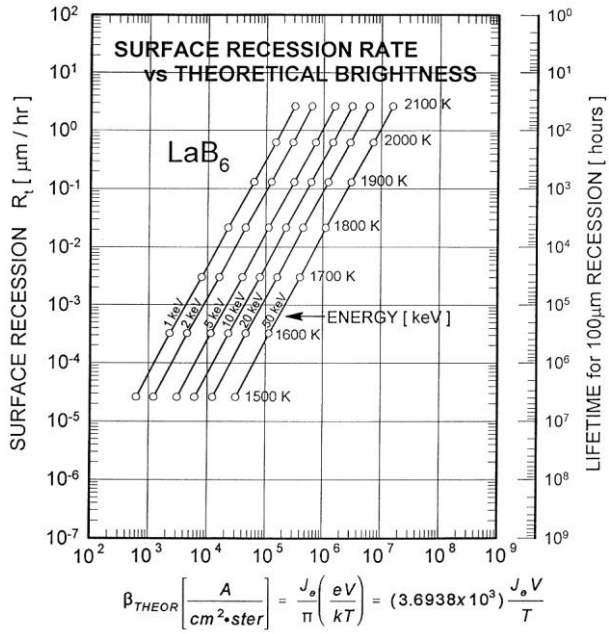

Figure 3.5. Brightness and evaporation rates for LaB6 cathodes at different temperatures and acceleration voltages. Adapted from [51].

The brightness of an electron beam is customarily expressed in Amperes per solid angle and unit area. The thermally limited e-beam brightness is given by

$$\beta_e = \frac{\rho_c e V}{\pi k_B T}, \tag{3.3}$$

where ρ_c is the cathode current density, e is the electron charge, V is the acceleration voltage, k_B the Boltzmann constant and T the cathode temperature. Some conclusions can be directly drawn from Eq. (3.3): The limiting value of brightness is directly proportional to the emitted current density, inversely proportional to the cathode temperature and that acceleration increases the brightness linearly. However, as shown in Sect. 3.2.2, for a thermionic source the cathode current density increases exponentially with the temperature and therefore the net effect of raising the temperature is to increase the brightness of the electron beam. The evaporation rate of the emitter material also increased with the temperature, thus setting a maximum operating temperature consistent with a

useful lifetime. Figure 3.5 illustrates typical performance of LaB_6 cathodes in terms of lifetime and brightness.

Equation (3.3), derived for the simple case of parallel acceleration, has in fact a much wider implication. It represents the fundamental limitations to the brightness obtainable in an electron gun. The brightness cannot be increased irrespective of any focusing system that may follow the gun. This can be illustrated by considering a simple focusing system of magnification M, which increases the current density M^2 times and increases the angular aperture by $1/M^2$, thus leaving the brightness unchanged.

The brightness limit can also be derived using rigorous statistical mechanical treatment involving Liouville's theorem, for a general electro-optical case.[52,53] For the case of laser driven or a field emission based cathodes, a somewhat different approach has to be used to derive the brightness limitations [54], but this will not be discussed further in this Thesis.

3.4.1 Brightness Limited Power Density

The goal in any electron-impact x-ray tube is to convert the electron beam brightness to power density on the target. This can be simply calculated by

$$\omega = \pi \beta_e \alpha^2 V, \tag{3.4}$$

where ω is the power density, β_e is the brightness of the electron source, α the focusing angle and V the beam acceleration voltage. The minimum, brightness limited, spot size diameter, d_β can be calculated with

$$d_\beta = \sqrt{\frac{4I}{\pi^2 \beta_e \alpha^2}}, \tag{3.5}$$

where I is the beam current, calculated using Eq. (3.1). Figure 3.6 shows that high power densities at small spot sizes are in principle achievable with a high brightness electron source. Furthermore it shows that in an ideal electro-optical system the achievable power density is set by the cathode brightness and the focusing angle. As we will see later, other factors, such as aberrations (cf. Sect. 3.6.2) and electron scattering (cf. Sect. A.1 and 4.6) limit the achievable power density and the subsequent x-ray brightness.

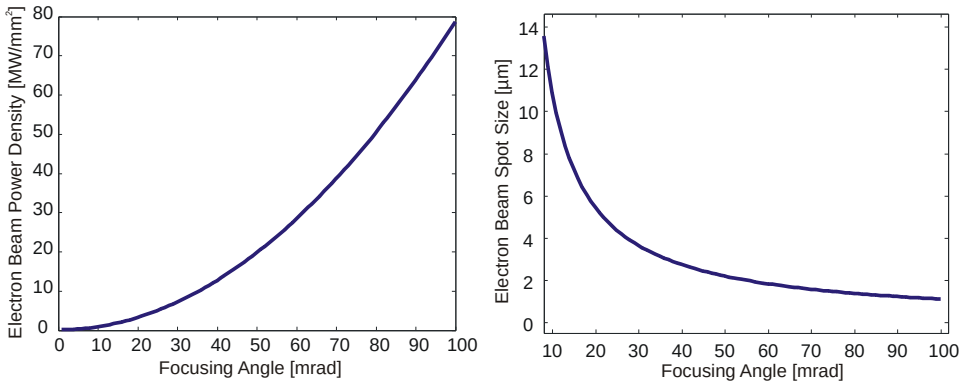

Figure 3.6. Brightness limited power density and spot size calculated for a 50 keV electron beam assuming a 50 µm diameter LaB_6 cathode at 1925 K ($\beta \sim 5\times10^6$ [A/cm²/sr]).

3.4.2 Emittance

Another quantity closely related to the brightness is the emittance, which is a measure of the parallelism of a beam. [55,56] Emittance is, as brightness, conserved in an optical system and is a commonly used for beam quality characterization. The phase space area of a beam in a rotationally symmetric system can be expressed in radial and angular coordinates, also known as the trace space. The same reasoning that was used in the derivation of Eq. (3.3) yields a minimum trace space area for a thermally limited electron beam.

$$\epsilon_{thermal} = r_c r_c' \text{ [π mm mrad]}, \tag{3.6}$$

where r_c, is the radius of the emitting source and $r_c' = \left(\frac{\pi k_B T}{eV}\right)^{\frac{1}{2}}$ is the divergence caused by the thermal velocity distribution of the electrons. The thermal emittance represents the minimum achievable phase space volume using a thermionic cathode. The following relationship between emittance and brightness holds for isotropic beams with average emittance, ϵ

$$\beta \cong \frac{I}{\pi\epsilon^2}, \tag{3.7}$$

where I is the beam current. Small emittance values can be achieved by using a small source, i.e., by reducing r_c or by lowering the initial transversal velocity, i.e., by lowering the temperature for thermionic sources. One cannot, however, indefinitely reduce the radial dimensions of the source, as self-field (space-charge) forces depend on the beam volume (cf., Sect. 3.5) and can potentially nullify any

gain achieved by size reduction. This leads one to use high electric field gradients to quickly accelerate the thermal electrons to relativistic energies.

The emittance concept is a powerful tool for analyzing the beam quality and for making rough estimates of expected performance. Figure 3.7 shows a schematic sketch of a simple electro optical system based only on emittance calculations. The product of beam angle and radius is conserved and the only parameters needed for making good performance estimations is the source emittance and the maximum focusing angle that can be used.

Accurate ray-tracing can yield information about the beam quality and Fig. 3.8 shows emittance graphs calculated using Lorentz2D-EM (cf. Sect. 3.7) for the high power electron beam used in Paper 6. The left panel displays the radial-angular particle distribution for the beam just after the acceleration gap, showing minor distortion due to perturbations from imperfect acceleration fields and space charge. The right panel shows the same beam after the beam focus, displaying large distortions due to non-linear focusing forces induced by spherical aberrations in the magnetic lens. The emittance is the area of the ellipse that encloses all of the electrons in trace space and it is clear that this quantity has grown after focusing.

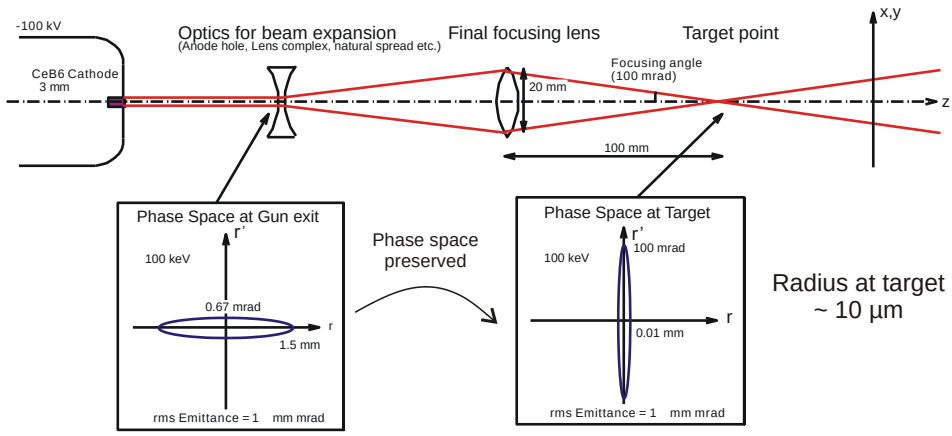

Figure 3.7. Electro optical design based on emittance considerations. Adapted from [57].

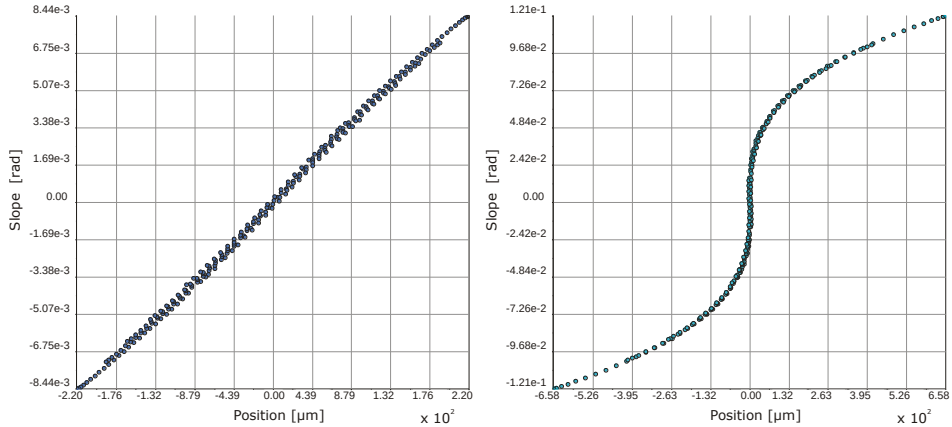

Figure 3.8. Left: Emittance graph of a beam right after the acceleration gap. Right: The beam after focusing with a magnetic lens showing distortion of the trace due non-linear focusing.

3.5 Space Charge

High brightness operation of an electron gun requires maximum beam throughput. A large total beam current is often needed, which results in increased electron-electron interactions. [58] This will have a number of consequences that will affect the imaging properties of the electron optics:

i. *Space-charge limited current,* a fundamental limit setting the maximum current that can be extracted from a cathode.

ii. *Space-charge defocus*, the self-field created by the beam has a defocusing effect. Increases the beam divergence.

iii. *Trajectory displacement effect,* increases the average transversal velocity component of the beam and can consequently lead to lower beam brightness and blurred focusing. Cannot be fully corrected with optics. [59]

iv. *Boersch effect,* an effect that increases the energy spread of the electrons due electron-electron interactions. [60]

The *space-charge limited current* can be described with the Child-Langmuir law [44]

$$I_{scl} = \frac{4}{9}\epsilon_0 \sqrt{\frac{2e}{m_e}} \frac{S}{d^2} V^{\frac{3}{2}} F, \tag{3.8}$$

where V is the acceleration gap voltage, d is the gap distance, and S is the cathode area. In the case where the cathode radius is much smaller than d, the field enhanced emission has to be taken into account. The factor F is introduced to model the higher beam currents achievable with small cathodes and can be calculated with the methods from Ref 35. F is usually at least 10 for cathodes used in microfocusing systems.

The electric field generated by the electron beam, also known as the self-field, does not only affect the maximum extractable current, it also causes broadening of the beam, or *space-charge defocus*. This can have adverse effects on a system since the divergence increase will be a function of the beam current and voltage. If the beam size increases much it might start hitting the walls of the vacuum envelope, causing heating and reducing the beam throughput to the target. It can also lead to excessive aberrations if there are any focusing elements in the system (cf. Chap 5). The defocus can be corrected for a uniform charge distribution in an axially symmetric beam by re-focusing.

For really high-current or low-energy beams, the strong self-repulsion of the beam can limit the minimum achievable spot size. This focusing limit for a charged beam with an envelope radius $r = r(z)$ can be examined via the envelope equation [100]

$$\frac{d^2 r}{dz^2} = \frac{e}{2\pi\epsilon_0 m_e c^3} \frac{I}{\beta\gamma} \frac{1}{r} = \frac{2I}{(\beta\gamma)^3 I_0} \frac{1}{r}, \tag{3.9}$$

where I is the beam current, I_0 is the Alfvén current and with β and γ being the usual relativistic factors. The minimum beam radius in a focusing system can be derived from Eq. (3.9) and is defined by

$$r_m = r_0 exp\left\{-\frac{(\beta\gamma)^3 I_0}{4I}\alpha^2\right\}, \tag{3.10}$$

with α being the focusing angle and r_0 the beam radius at the focusing element. Evaluation of Eq. (3.10) for currents in the range of 1-100 mA, beam energies of >50 keV and for focusing angles >50 mrad (r_0 set to 1 mm), lead to a sub 1 μm radius. Thus, the space charge effect, in terms of focusing limitations, can be neglected to a good approximation for microfocusing systems.

In addition to the effects already mentioned, the energy spread/chromacity of the electron beam can grow larger than what is predicted from the thermal agitation at the cathode ($\approx k_B T$). This energy spread is caused by the stochastic coulombian interactions between the electrons in the beam and is called the *Boersch effect*.

The space charge effects described above are strongest close to the cathode, where the electron velocity is lowest and the charge density is high. If a high brightness electron beam is to be generated, careful design of the acceleration gap is required. Once the beam is fully accelerated other effects, such as aberrations and beam brightness rather than space charge, are generally dominating the beam quality and focusing properties.

3.6 Electron Optics

Once an electron beam has been created, magnetic and electric fields can be used to focus, deflect and in other ways manipulate the beam into the desired shape and size. For electron impact based x-ray generation, where the x-ray brightness is directly proportional to the electron beam power density, the beam is formed into a focused spot, as intense as the target system can handle.

The equation of motion for charged particles is governed by the Lorentz force law [61]

$$\frac{d\bar{p}}{dt} = q(\bar{E} + \bar{v} \times \bar{B}), \tag{3.11}$$

where $\bar{p}$ is the relativistic momentum, q the electron charge, $\bar{E}$ the electric field, $\bar{v}$ the particle velocity and $\bar{B}$ the magnetic field. The field distributions needed to calculate the electrons trajectories are generally too complicated to solve with analytical methods and numerical techniques are used to acquire the values. [62-66] The various methods will be briefly discussed in Sect. 3.7.

Magnetic fields are used in wide range of applications for beam manipulation and focusing. Since the force generated by magnetic fields is always orthogonal to the velocity vector of the electrons, the energy is always conserved. A magnetic field is created by an electrical current and multi-turn coils are used to create the needed current density. The coil is commonly surrounded by field conducting magnetic materials which are used to enhance the field strength and to confine the field into a well defined region. [67] By modifying the yoke geometry, the spatial field distribution can be manipulated to the desired shape. [68,69] The maximum field strength that can be generated is limited by the magnetic saturation limits of the

material used for the yoke. [70] Magnetic lenses typically have reduced aberrations compared to electrostatic optical elements, and are thus preferred in high performance applications. [71] One of the consequences of energy preserving properties of charged particles in magnetic fields is the rotation of the beam, illustrated in Fig. 3.9 where a beam of electrons have been ray-traced through a focusing electromagnet.

Electrostatic field distributions are determined by the geometrical shape and charge distribution of the conductor used to generate the field. They are commonly used in applications where space is premium and the electron-optical performance is not critical. [72] The major issue with electrostatic lenses is the practical problems connected with the generation of high voltages and the requirement of placing them inside the vacuum system. Electrostatic lenses have generally aberrations that are an order of magnitude higher than for an equivalent magnetic lens. Both types can be found combined in advanced electro-optical systems, with the reduced aberrations as a result. [47]

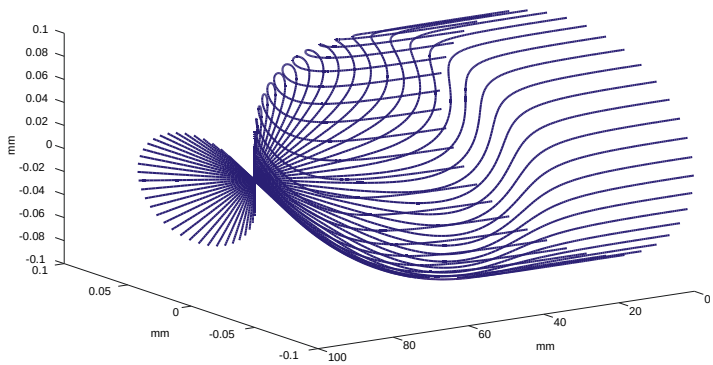

Figure 3.9. Electron ray-tracing through a focusing magnetic field showing a characteristic rotation in the field. Only the envelope rays are shown here.

Both magnetic and electrostatics elements can be sorted by their geometrical shape and the type of beam manipulation they are typically used for

i. *Rotationally symmetric.* Equivalent to round lenses commonly found in visible light optics. By far the most common electro-optical element, used for focusing and image forming.

ii. *Dipole.* A geometry that induces fields used for beam deflection or line forming. Equivalent to mirrors or cylinder lenses in optics

iii. *Multipole*. Used for strong focusing (quadruple) or aberration reduction (hexapole, octopole, etc.).

Figure 3.10 illustrates some of the most common electro optical elements. In electron guns for x-ray generation in the microfocus range, the optics usually consists of at least one rotationally symmetric focusing lens. Beam deflection and alignment elements are also common. A few tubes use quadruple lenses for line focus forming and astigmatism correction. [73] Figure 3.11 depict two high-end microfocusing systems, with the magnetic lens based optical column shown in detail.

Figure 3.10. From left to right: rotationally symmetric, dipole (X-deflection), double dipole(X-Y deflection), line focusing double dipole/quadrupole, sextupole element.

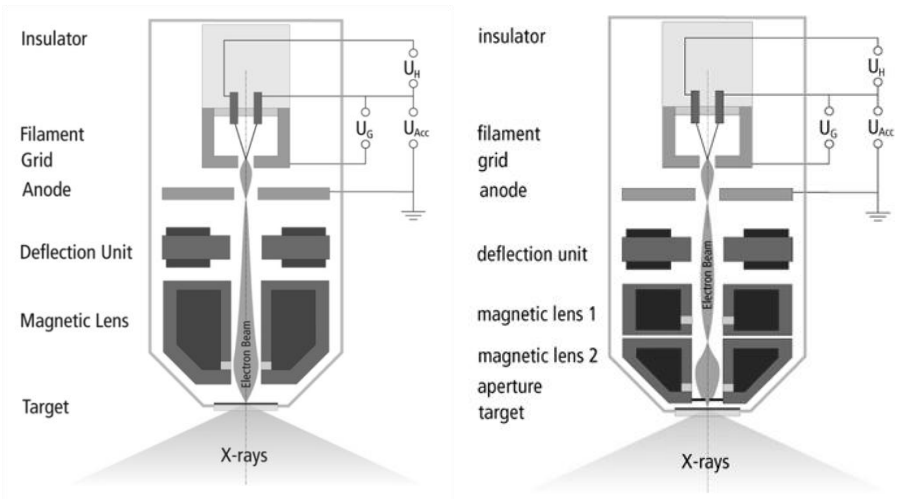

Figure 3.11. A microfocus and nanofocus x-ray transmission target tube (cf. Sect. 4.4). Adapted from [74].

3.6.1 Aberrations

Any electrostatic or magnetic field with rotational symmetry has imaging properties. Electrons starting from a point in the cathode plane are imaged into a point in the image plane. In an ideal optical system, stigmatic, or point-to-point imaging is

achieved. Unfortunately, electro-optical focusing or imaging systems are far from perfect. They suffer from aberrations. The effect of non-linear forces can be treated using aberration theory, which is used to describe the perturbations causing an optical system to deviate from stigmatic image formation. [75]

Aberrations can be roughly classified as follows:

i. *Axial aberrations:* Spherical and chromatic.

ii. *Off-axis aberrations:* Coma, astigmatism.

iii. *Field aberrations:* Field curvature, distortion.

The aberrations that are relevant in a well-aligned focusing system are the non-vanishing axial aberrations, namely spherical and chromatic aberration. The spot size enlargement due to spherical aberration can be expressed as

$$d_s = \frac{1}{4} C_s \theta^3, \tag{3.12}$$

where C_s is the aberration coefficient and θ is the focusing angle. Figure 3.12 illustrates the action of positive spherical aberration; peripheral rays are more strongly focused than the paraxial, thus creating a blurred focus.

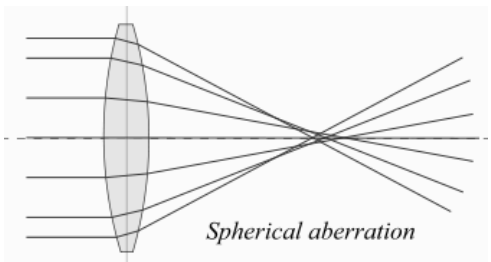

Figure 3.12. Spherical aberration illustrated with a glass lens.

For chromatic aberration we have that

$$d_c = \frac{1}{4} C_c \frac{\Delta V}{V} \theta, \tag{3.13}$$

where C_c is the aberration coefficient, $\frac{\Delta V}{V}$ the monochromacity ($\Delta V \sim 0.1 - 1$ eV) of the beam, and θ is the focusing angle. The contributions d_s and d_c are the aberration disk diameters at the circle of least confusion, where the aberrated beam

envelope has its minimum radius. The disks are a factor of 4 larger in the paraxial image plane. A common method of quickly estimating the final focus size [76] is to calculate the square root of the quadratic sum of the aberration disks and the brightness limited spot size, d_β

$$d_{total} = \sqrt{d_\beta^2 + d_c^2 + d_s^2}\,, \tag{3.14}$$

where d_β is just the de-magnified image of the electron source, limited in size by the beam brightness, cf. Sect. 3.4.1. If the exact intensity distribution is required or if the focus is very small, i.e., in the micro or nanometer range, more advanced methods [77,78] are needed since the aberrations have very un-Gaussian intensity distributions (cf. Chap. 5). Then the results gained from Eq. (3.14) can be misleading in terms of achievable resolution and contrast, both in x-ray generating systems and electron microscopes. [79,80,81]

Of the two axial aberrations, the spherical aberration is generally by far the one contributing most to spot size due its cubic growth with focusing angle. The energy spread and the subsequent chromatic aberration of a well-designed electron gun, using a tightly regulated high voltage and lens power supplies, is small. Thus, chromatic aberration is generally not a major contributing factor to focus enlargement in microfocusing systems.

3.6.2 Aberration-Limited Power Density

The evaluation and optimization of aberration coefficient for different electro optical elements and their effect on the resolution and image quality have been studied extensively over the years, both analytically [82,83,84] and numerically. [85,86] Section 3.7.4 describes some numerical methods that can be used to evaluate the aberration coefficients.

Using Eq. (3.14) in conjunction with Eq. (3.5), the spot size of a finite brightness electron beam using focusing elements with aberrations can be estimated. Figures Figure 3.13 and Figure 3.14 illustrate the spot size and power density as a function of the beam focusing angle. Figure 3.13 shows a simulation for a lens with C_s =3.8 cm and Fig. 3.14 a lens with C_s =1 cm. The optimal focusing angles, where maximum power density is achieved, are ~40 mrad and ~60 mrad, respectively, for the two investigated lenses. The spot size and power density for both lenses was calculated assuming a 50 μm LaB_6 cathode operated at 1925 K with an emission current of ~1.2 mA at 50 keV.

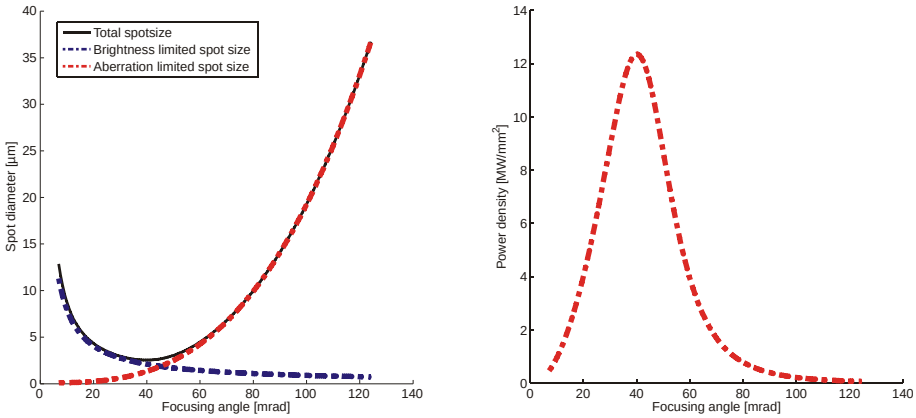

Figure 3.13. Left: The spot size as a function of the focusing angle for a lens with C_s = 3.8 cm. Right: The power density as a function of the focusing angle

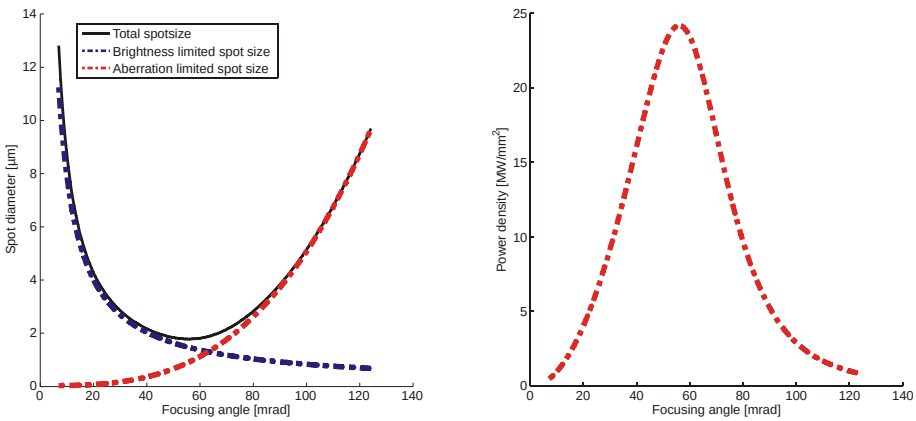

Figure 3.14. Left: The spot size as a function of the focusing angle for a lens with C_s = 1 cm.. Right: The power density as a function of the focusing angle

The conclusion that can be drawn from these figures is there exists an optimum focusing angle which is dependent on the brightness of electron source and the properties of the focusing element. Furthermore, the figures show that reducing the spherical aberration coefficient allows for higher power densities.

For best performance, the optimum angle should be achieved in the whole power range of the gun. As we will see later in Chapter 5, this is not possible to achieve in a single lens system where maximum beam throughput is required and beam angle defining apertures cannot be used.

3.6.3 Aberration Correction

In visible light optics fully aberration-corrected optical elements are readily available. Unfortunately, the intrinsic aberrations of electro-optical elements are much larger than what is found for visible light lenses. Focusing angles are typically restricted to much less than 100 milliradians, equivalent to a numerical aperture (NA) of ~0.1. This should be compared with fully corrected visible light objective lenses that can have NA's of up to 1.4. Despite the difficulties faced due to the aberrations, early researchers succeeded in creating powerful instruments such as the SEM, TEM and STEM, capable of probing the atomic world.

Scherzer [87,88] showed early (1936) that rotationally symmetric magnetic and electric lenses always have non-vanishing positive spherical and chromatic aberration coefficients. Thus, it is very difficult to correct for the aberrations using methods common for visible light optics, i.e., aspherical lenses or lens combinations where the total aberrations could cancel. Understanding the limitations imposed by the aberrations, Scherzer also suggested the use of multipole lens elements as a possible solution for aberration correction. Unfortunately electronics and manufacturing techniques were not advanced enough at that time and the improvements gained were very small. Modern, high precision electronics, higher machining tolerances and powerful computers have recently enabled the design and implementation of aberration corrected optical columns although the systems are still too expensive and complicated for common use. [89,90]

3.7 Numerical Methods

A number of numerical tools are available for electric and magnetic field analysis. Most of them are based on finite (FEM) or boundary (BEM) element techniques and further information and details about the different methods could be found in Refs 27 and 91-93. By proper assignment of boundary conditions and material parameters, Maxwell's equations can be solved with high accuracy. With the significant computing power readily available today, extremely accurate field solutions can be generated even in complex 3D geometries enabling systematic optimization of complete electro-optical systems. [94-97]

When designing and optimizing electron guns and electron optics, specialized software with the additional capability to simulate different electron emission regimes, space charge effects and ray tracing is needed, and Lorentz2D-EM [98] was used for most of the work presented in this Thesis.

3.7.1 Space Charge Effects

The accuracy of the field solutions and the ray tracing is most critical in the acceleration gap, where the electron beam is sensitive to any perturbations and the space charge forces are strongest. Figure 3.15 illustrates a typical simulation result using Lorentz2D-EM, where the space charge effects of a 1.53 mA beam in a 50 kV acceleration potential is investigated. The electron source is a LaB_6 guard ring cathode at 1950 K. Figure 3.15b shows how the strong diverging effect caused by space charge is expanding the beam from a starting radius of 25 μm to ~ 215 μm over a distance of ~24 mm.

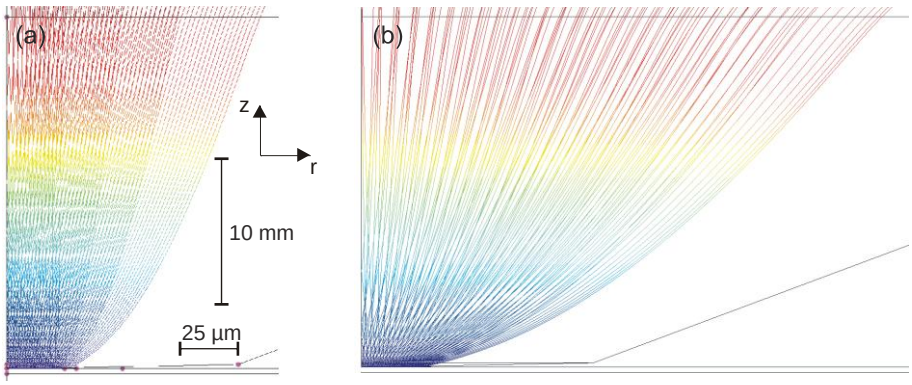

Figure 3.15. a) An accelerated beam with only thermal divergence showing. **b)** An accelerated beam with both thermal and space charge effects showing. The color of the rays represent their increasing energy during the acceleration. The brightness of the simulated beam is $7.3 \times 10^6\ A/cm^2/sr$ with a current density of $77\ A/cm^2$.

3.7.2 Paraxial Beam Equation

Although complete electro optical systems are possible to simulate using dedicated software such as Lorentz2D-EM, their main strength of these programs is in the possibility of detailed analysis and verification of specific scenarios. The time and effort required to design and optimize an arbitrary optical system is still extremely demanding. A more efficient method of designing electro optical systems is by generating high- accuracy field solutions for the optical elements used in the system, using any of above mentioned software implementations and then using these fields as input for faster and simpler ray-tracing methods.

Most of the relevant optical properties can be studied using the paraxial ray equation. [99] In particular, the cardinal elements (principal, focal and image planes) of the optics and first order-aberrations can be solved, giving quick and valuable

feedback in the design process. As only the field values at the optical axis are required, very fast ray tracing is possible, enabling efficient parametric optimization of an electro optical system. The paraxial ray equation for rays in magnetic and electrics fields can be expressed as

$$r'' + \frac{q}{8m_eV}B^2r + \frac{\Phi'}{2\Phi}r' + \frac{\Phi''}{4\Phi}r = 0, \tag{3.15}$$

where $r(z)$, $r'$and r'' is the ray radius and its derivates, taken with respect to z, $B(z)$ the axial magnetic field, $\Phi(z)$, Φ' and $\Phi''$the axial electrical field and its derivates. By tracing a ray with the initial conditions, $r = 1, r' = 0$, the location of the focal and principal planes can be found out. An additional ray traced with initial conditions, $r = 0, r' = 1$, enables the coefficients for C_s and C_c to be found, see also Fig 3.16. The focal length and the magnification of an optical element can now be calculated. Although a lot of information about the optical properties can be gained from using Eq. 3.15, it doesn't give any information about the effects of space charge or the limits imposed by the finite brightness of the electron source.

3.7.3 Beam Envelope Equation

Another valuable tool for understanding the beam dynamics is the relativistic beam envelope equation [100], which is similar to the paraxial ray equation but with additional terms for space charge and finite brightness effects. It reads

$$\mathrm{r}'' + k^2r + \frac{\gamma'}{\beta^2\gamma^2}r' - \frac{2I}{\beta^3\gamma^3I_0r} - \frac{\epsilon_\mathrm{N}^2}{\beta\gamma r^3} = 0, \tag{3.16}$$

where the second term represents the effects from magnetic fields, the third beam acceleration, and the fourth space charge, where I is the beam current and $I_0 = \frac{4\pi\epsilon_0 m_e c^3}{q}$ the Alfvén current and with the last term representing the finite emittance of the beam, with ϵ_N being the normalized thermal cathode emittance. β and γ are the usual relativistic factors. ϵ_N can be calculated via simulations of the acceleration gap using Lorentz2D-EM or analytically with

$$\epsilon_N = 2r_c\sqrt{\frac{k_BT}{m_ec^2}}. \tag{3.17}$$

Equation (3.16) is unfortunately not applicable if the electrons have radial velocities comparable to the velocity in the direction of the beam axis. This due to beam

laminarity conditions assumed in the derivation of Eq. (3.16), not valid for slow electrons in strong self-fields, i.e., close to the cathode. [101] For accurate results, the beam should be simulated using more advanced methods (e.g., Lorentz2D-EM) in the acceleration gap.

3.7.4 Calculation of Aberration Coefficients

There are a number of different methods that can be used to analyze and extract the aberration coefficients. The accuracy of all the methods is highly dependent on the quality of the field solution.

Direct ray-tracing, using software such as Lorentz2D-EM, can yield aberration coefficients up to a high order. [102] By simulating a monochromatic point source located in the cathode plane and tracing the rays to the image plane, the spherical aberration coefficient, C_s, for an optical element can be calculated. Figure 3.16 (left) illustrates the axial deviation of the rays near the paraxial focus as a function of the focusing angle for a magnetic lens. By adapting a polynomial curve to the data, the coefficient, C_s, can be found, and is 3.8 cm in this case. The chromatic aberration coefficient can be extracted in a similar way by ray-tracing a point source with an energy spread and constant take-off angle from the cathode plane. The main problem with the direct ray-tracing method is the significant computational requirements necessary to get reliable resultants.

By using the solution to the paraxial ray equation, Eq. (3.15), the first-order aberration coefficients can be directly computed by evaluating suitable integrals. [103] For example, the formulae for computing the spherical and chromatic aberration coefficient, C_s and C_c, respectively, referred to the image plane z_i are

$$C_s = \frac{e}{128 m_e V} \frac{1}{r'^4(z_i)} \int_{z_o}^{z_i} \left(\frac{3e}{m_e V} B^4 r^2 + 8B'^2 r^2 - 8B^2 r'^2 \right) r^2 dz, \tag{3.18}$$

and

$$C_c = \frac{e}{8 m_e V} \frac{1}{r'^2(z_i)} \int_{z_o}^{z_i} B^2 r^2 dz, \tag{3.19}$$

where $r(z)$ is a paraxial ray that starts from the optical axis at the object plane z_o, and crosses the axis again at the image plane z_i. Similar formulae can also be used to compute the off-axis and primary field aberrations. The aberration integrals are highly suitable for parametric analysis and optimization of electro-optical elements. Since only the field values on the optical axis are required for the integrals, fast and accurate results can be generated. The right panel of Fig. 3.16 shows a simulation

result where the optical properties of a magnetic lens are investigated. By using Eqs. (3.18) and (3.19) in combination with Eq. (3.15), all the relevant properties of a focusing electro-optical element can be calculated.

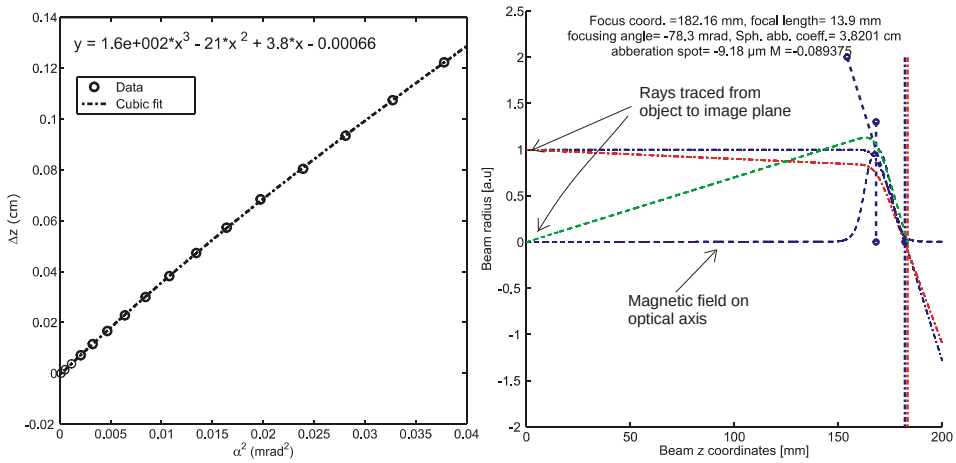

Figure 3.16. Left: The spherical aberration coefficient for a magnetic lens, calculated by direct ray tracing in Lorentz2D-EM. **Right:** The paraxial equation is used to calculate the cardinal elements and aberration coefficients of a magnetic lens. Three test rays from the cathode plane (z=0) are traced though a magnetic focusing field, illustrated with a dashed blue line along the optical axis, to the image plane. The two vertical lines represent the image and focal planes. The principle plane is shown as a short vertical line close to where the magnetic field is at its maximum.

Chapter 4

Electron-Impact Target Properties

In this chapter the other critical component of the electron-impact x-ray system, the liquid-jet target, is studied in detail. A comparison of the liquid-jet target with conventional solid targets is made. In addition some of the experimental results and methods used in Papers 1-6 are presented.

4.1 Solid vs. Liquid-Jet Targets

In electron-impact-based x-ray tubes the generated x-ray brightness is directly proportional to the applied electron-beam power density on the target. X-ray production via electron impact is an inherently inefficient process and most of the absorbed energy (~99%) is converted to heat. The target is commonly a high-Z, high-melting-point metal plate with good thermal properties. In terms of achievable x-ray brightness these requirements restricts the available materials to refractive metals such as, e.g., tungsten. Tungsten combines good thermal properties with a high atomic number, making it an efficient x-ray generator (c.f. Appendix A) and is by far the most popular target material in conventional x-ray tubes. For applications requiring line radiation at specific energies, other material can be used, such as; molybdenum/rhenium (mammography), silver, copper, chromium (crystallography) or silicon (EUV). In these cases performance in terms of bremsstrahlung emission efficiency is traded for more radiation at the energy required by the application.

Solid-anode x-ray tubes are thus limited in x-ray brightness due to the thermal properties of the anode material. The temperature of the target must be kept well below the melting point of the material in order to avoid damage and serious performance degradations. Substantially higher e-beam power densities and subsequently higher x-ray brightness is possible to achieve using high brightness electron guns as discussed in chapter 3. In order to utilize this, a thermally less sensitive target is needed. A liquid-jet-based e-beam target fulfills the required thermal robustness.

An electron-impact target can be characterized in terms of three parameters, namely, thermal (power density and x-ray brightness), mechanical (speed and stability) and geometric (self-absorption and accessible spatial angle of x-ray emission). By examining each of them in turn and comparing to conventional target technology, the advantages of using a jet target is clarified.

4.2 Thermal Properties and Power Load Capacity

The power load of stationary targets scales approximately linearly with the e-beam focus area.[9,104,105,106] Hence, reduction of the source size is an effective means of increasing the x-ray brightness, see also data for tubes # 8-14 in Table 4.1. Grider [107] showed that the heat load capacity, expressed in watts per e-beam diameter, is in the range of 0.4-0.8 W/μm for microfocus systems, i.e., ~4-8 W of e-beam power in a 10 μm spot, corresponding to a power density of ~50-100 kW/mm^2. These values are achieved assuming that high melting point and/or high-thermal-conductance materials, such as Cu, W or Mo, are used. In most cases, low brightness, W cathode based electron guns can easily generate the power densities (cf. Table 3.1 in Sect. 3.2) matching the maximum target load capacity. However, high-end microfocus and nanofocus x-ray tubes, using transmission targets with spots <1 μm, can be found using LaB_6 based cathodes. [34] This is due to the short life time of W based cathodes when operated at e-beam brightness levels matching the target loading capacity for sub 1 μm spots.

The maximum power density for millimeter sized spots, commonly used in radiography applications, is orders of magnitude lower, typically <1 kW/mm^2 for stationary and <10 kW/mm^2 for rotating anodes with > 1 mm^2 sized spots. The apparent power density can be increased by a factor of ~4-8 from these numbers by using line focusing. We note that these peak power densities for rotating anode systems can only be maintained during short exposure times with a cooling-down period customarily required between exposures. The lifetime of solid target tubes, including microfocus systems, is set by the condition of the target surface, which deteriorates with time due to thermal stresses and damage, leading to a gradual reduction of the x-ray flux and quality over time. Table 4.1 shows the thermal power load capacity and x-ray brightness of a range of x-rays tubes used for crystallography with the liquid-jet-target source added for comparison. The brightness of the solid-target sources are for the Cu K_α line (8 keV). The specifications for the jet-target x-ray source (#15) are based on data from a commercial prototype and the quoted brightness is for the Ga K_α line (9.2 keV) from a Galinstan jet. [108]

X-ray tube power loading and brightness.

#	Power	e-beam incident angle	Focal spot		Takeoff angle	Target speed	Power loading			Brightness
			Length	Width			real	Calculated	relative	
	kW	degrees	mm	mm	degrees	m/s	kW/mm^2	kW/mm^2	kW/mm^2	photons / sec mm^2 mrad^2
Rotating anode x-ray tubes										
1	18	90	10	0.5	6	31	3.6	12.8	0.28	1.1E+09
2	5.4	90	3	0.3	6	31	6.0	16.5	0.36	1.8E+09
3	3	90	2	0.2	6	31	7.5	20.2	0.37	2.2E+09
4	1.2	90	1	0.1	6	31	12.0	28.5	0.42	3.5E+09
5	0.8	90	0.7	0.07	6	31	16.3	34.1	0.48	4.8E+09
6	5	90	1.5	0.15	6	118	22.2	45.6	0.49	6.5E+09
7	3.5	90	1	0.1	6	118	35.0	55.8	0.63	1.0E+10
Stationary target x-ray tubes										
8	2	90	10	1	6	0	0.2	0.3	0.60	5.8E+07
9	1.5	90	8	0.4	6	0	0.5	0.7	0.67	1.4E+08
10	0.8	90	8	0.15	6	0	0.7	1.5	0.44	1.9E+08
11	0.035	90	0.2	0.02	6	0	8.8	16.6	0.53	2.6E+09
12	0.03	78	0.14	0.02	8	0				2.6E+09
13	0.01	45	0.02	0.0135	45	0	38.8	49.1	0.79	3.2E+09
14	0.0012	90	0.002	0.002	6	0	300.0	391.5	0.77	9.2E+09
Liquid-jet target x-ray tubes										
15	0.1	90	0.01	0.01	0	>50	~1200	-	-	>1.0E+11

Table 4.1. Adapted from [109].

The basic reason for the superior performance of the liquid-jet-target is that the target is regenerative. In contrast to solid targets, liquid-jets can in principle be heated up to the complete evaporation of the material. Stable operation of a fully evaporated methanol jet is demonstrated in Paper 6 and metal jets should be possible operate under similar conditions although the debris generation and its mitigation would pose a significant engineering challenge, cf. Paper 3. In Papers 3-5, various metal jets were operated stably at significantly higher e-beam power loads (up to 8 W/μm) than customarily used in solid-target systems. It should be noted that the gun was intentionally operated at reduced power levels in order to keep debris rates manageable, mainly due to the lack of a debris mitigation system and the relatively low jet speeds used.

Liquid-jet sources can, in contrast to solid target sources, also be operated at peak brightness for extended periods. This could be a distinct advantage in applications requiring longer exposure times such as phase contrast imaging, microtomography and crystallography. In addition, jet targets can be created using a wider range of materials and where the limitation is set by the amount of elements found in liquid form at reasonable experimental conditions. Even though metal jets generally have a higher heat-load capacity and x-ray generation efficiency, non-metallic jet materials extend the number of available characteristic lines, especially in the lower range of the x-ray spectrum. Furthermore, such liquid-jets generally produce

vaporization products that can be directly pumped from the vacuum system. However, the chemical reaction of the vapor products with the electron gun cathode must be considered, especially for oxygen and carbon compound containing vapors, which are known to influence the lifetime of the cathode.[110,111] The partial pressures of such gases in the vicinity of the cathode could be reduced to a large degree by a properly designed differential pumping scheme. For instance, environmental electron microscopes (ESEM) are routinely operated with large differential pressures between the sample (~1 mbar) and electron gun chamber (~1×10^{-9} mbar). [112]

4.3 Target Speed and Stability

Rotating anodes have so far only been reported for spots down to ~70 μm [113], probably due to difficulties maintaining good mechanical stability at high rotation speeds and avoiding surface roughness induced by thermal stresses in the target material. Rotating anodes are mainly used for high-flux applications in general radiography although some variants with relatively small spots and lower powers are used as dedicated crystallography tubes. Target speeds of up to ~118 m/s [114] have been reported with rotating anodes. Further improvements in rotation speed seems difficult to accomplish. [10]

The speed and stability of a liquid-jet-based target is governed by the fluid mechanical properties of the liquid, the geometry of the liquid-jet-producing orifice and the ambient conditions. In order to produce a coherent, directionally stable, microscopic, high-speed jet in vacuum these parameters have to be understood and controlled. Any given jet can described by four dimensionless fluid mechanical parameters: the Reynolds number (a measure of the probability of onset of turbulence), the Ohnesorge number (describes the influence of viscous forces), the Mach number (indicated whether the fluid can be considered to be in an uncompressed state), and the Weber number (determines the influence of the ambient atmosphere on the jet stability).

In Paper 2 we showed, with dynamic similarity experiments using water jets, that extremely fast metal jets (~500 m/s) should be possible to generate, although the pressures needed (~10000 bars) for such jets is likely to be a engineering challenge.

4.4 Geometrical Effects

The target in conventional x-ray tubes is a polished, flat metal piece, sometimes actively cooled with circulating water or forced air. In order to utilize line focusing,

the target is usually slanted at an angle with respect to the impinging electron beam. Figure 4.1 illustrates the geometrical differences between solid anodes and a jet based target. Line focusing distributes the heat load on a larger area and increases the effective power density by a factor of ~4-8, depending on the angle of view and spot size. [9] Since x-ray sources are not Lambertian emitters, a corresponding increase in brightness is gained. [115] Microfocus x-ray tubes generally use stationary targets and can be made very compact due to the simple design, making them suitable for applications where space and mobility are prioritized. For generation of < 1 μm x-ray spots, transmission targets are used, customarily consisting of a thin (~1 μm) tungsten layer deposited on low Z material such as beryllium or aluminum. [116-118] Transmission targets can suffer from reduced x-ray conversion efficiency due to significant electron beam transmission through the thin target. For bulk targets, a considerable amount of self-absorption for small viewing angles lead to reduced x-ray output and inhomogeneous radiation fields. This is also known as the Heel effect and reduces the usable x-ray collection angle. [119]

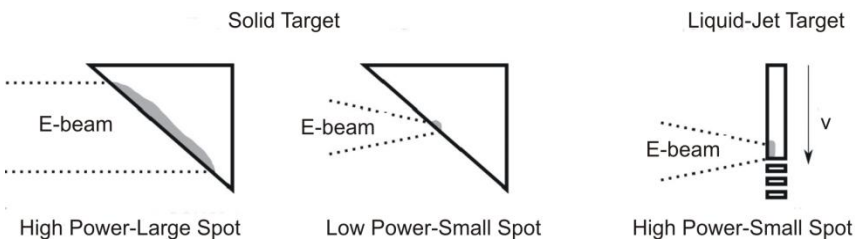

Figure 4.1. Schematic comparison between solid and liquid-jet targets.

Liquid-jets can assume a variety of forms depending on the shape of the jet-forming nozzle orifice. The liquid naturally forms droplets due to surface tension, minimizing its surface area. Typically we use cylindrical jets resulting in spherical droplets. However, the high speed allows for a relatively long distance from the nozzle where the jet is in a stable, and if needed, non-cylindrical form. Flat jets, for instance, could be more suitable if a line-shaped electron beam is used although a similar geometry could be accomplished with a large diameter jet. Considering cylindrical jets, which have been exclusively used so far, diameters can range from ~10 μm with the lower limit set by the practical issues connected to particulate clogging and with the upper limit set by the mass-transfer capacity of the pressurizing system and fluid-mechanical constraints. The x-ray self-absorption for small diameter jets is reduced and opens up the possibility to increase the usable x-ray collection angle to almost 4π.

To summarize:

- Jet targets can be operated at high speeds combined with a stability that enables enhanced performance in microfocus operation. Thus the liquid-jet-target enables moving target operation with spot sizes limited by electron scattering in the material. This in contrast to rotating anodes which have only been reported in operation for spots > 70 μm. Microfocus tubes with smaller spots are always based on stationary transmission or bulk targets.

- The regenerative nature of the jet target enables stable operation also at power and power-density levels that lead to total evaporation of the target. The practical feasibility is limited by the nature and amount of vapor products emitted from the jet, which can have detrimental effects on the electron gun cathode and the x-ray transmission if not mitigated. Stable, high power operation of high speed (~50-500 m/s) evaporating jets could potentially increase the x-ray brightness by at least an order of magnitude from the numbers reported so far.

4.5 Liquid-Jet Target Experimental Arrangement

Here the liquid-jet x-ray source experimental arrangement, shown in Fig. 4.2, and used in Papers 1 and 3-6, is described in more detail.

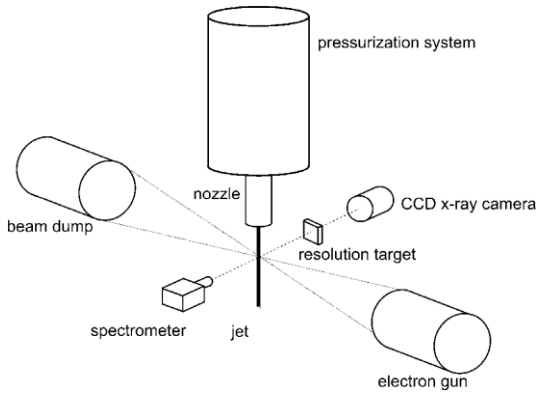

Figure 4.2. The proof-of-principle arrangement showing the major components and instruments used for source characterization.

The x-ray source with its nozzle arrangement for producing the liquid-jet target is situated in a vacuum chamber, which is pumped with a 500 *l*/s turbo-drag pump down to a base pressure of ~ 10^{-7} mbar. By applying up to 200 bars of nitrogen backing pressure a stable liquid-jet can be injected into the vacuum chamber via the tapered glass nozzle. The e-gun is based on custom-made 50-200 μm diameter LaB_6-cathodes with beam energies ranging from 10 to 50 keV with maximum powers of ~75 W (50 μm cathode) or 600 W (200 μm cathode). The beam is focused by a magnetic lens onto the jet resulting in a high-brightness x-ray spot. Chapter 5 gives more details about the performance of the gun. Differential pumping of the gun with a separate 250 l/s turbo-drag pump keeps the base pressure in the gun at ~10^{-8} mbar. The gun and jet chamber are separated by a 2.5 mm diameter anode aperture in the gun and a 6 mm aperture in the magnetic lens. The pressures in the gun and jet chamber generally rise to ~10^{-7} mbar and ~10^{-5} mbar, respectively, when operating the liquid-metal-jet x-ray source. These vacuum levels are low enough to get adequate transmission of the electron beam and the x-rays produced in the interaction with the jet.

A resolution target and an x-ray CCD camera with 9 μm pixels and a fiber optic coupling to a phosphor screen is used for imaging and source size

Jet Target Comparison				
Jet Material	Tin	Gallium	Methanol	Water
Melting point [K]	505	303	260	273
Operating temperature [K]	>550	>330	297	297
Jet diameter [μm]	>20	>20	>10	>10
Sp. heat capacity [$\mathrm{J\,kg^{-1}K^{-1}}$]	230	375	2500	4019
Heat of vaporization [$\mathrm{10^6 J\,kg^{-1}}$]	2.54	3.64	1.1	2.26
Jet velocity at 400 bars of backing pressure [m/s]	~100	~110	~310	~ 280
Average atomic number, Z	50	31	~7	~6
K_α line energy [keV]	25.3	9.25	0.277 0.525	0.525

Table 4.2. Liquid-jet-target parameters.

measurements. [120] The line-spread function (LSF) of the CCD camera is ~31 μm FWHM. A CdZnTe diode is employed for spectral flux measurements. [121] For jet inspection and stability studies, a long working-distance visible light microscope is used in combination with pulsed-laser illumination for high temporal resolution.

Table 4.2 displays information about some of the jets that we have used for x-ray generation. Data is shown for two metallic and two non-metallic jets. In addition to the jets presented in Table 4.2, metallic jets consisting of tin/lead (solder), bismuth, Rose's metal, Field's metal and Galinstan: (a gallium, indium, tin alloy) have been operated successfully. Although water jets haven't been investigated yet, it is included due to its good thermal properties and the possibility to generate characteristic line radiation in the water window, which makes the source a possible source candidate for soft x-ray microscopy. A Monte Carlo calculation estimating the possible brightness for a water-jet based soft x-ray source is found in Sect. 4.6.2.

4.5.1 X-Ray Source Characterization

As already noted, x-ray brightness is expressed as photons per second and per source area and spatial angle. Since electron-impact sources are generally polychromatic sources, the spectral brightness, which is just brightness per bandwidth, is also a useful quantity. In order to calculate spectral brightness, the spectrum and source size have to be accurately measured. The measured spectrum has to be compensated for absorption in the air and the beryllium windows along with corrections for exposure time, detector efficiency and spot size. For source size measurements, a number of methods are available. The following sections

describe the methods used for the source size measurements for the liquid-jet based x-ray system.

4.5.2 Pinhole Imaging

Pinhole imaging is based on the projection of the source through a circular aperture and can give good results if the x-ray source is much larger than the pinhole. The recorded image will be a convolution f the pinhole and the source intensity distribution and is, thus, limited in resolution to the size of the pinhole.[122] Since x-rays are hard to attenuate, the pinhole has to be placed on a relatively thick substrate which leads to problems with alignment using small pinholes due to high aspect ratios. Another problem is the very low level of the x-ray signal that is transmitted through the pinhole. One of the most useful applications for pinhole imaging is its use in aligning the electron gun. By studying the shape and intensity distribution of a defocused electron beam, the optical column could be adjusted for optimum performance, see Fig. 4.3.

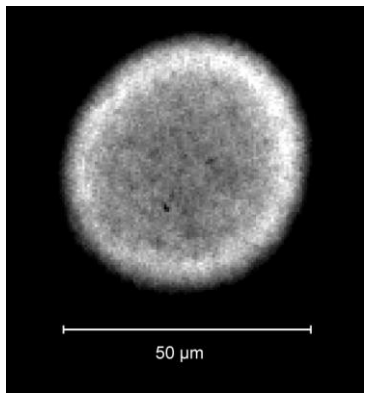

Figure 4.3. X-ray pinhole image, where the x-ray emission is generated by a defocused e-beam spot. Note the elevated intensity ring at the edge, characteristic of spherical aberration.

4.5.3 Edge Spread Measurements

By measuring the blurring of a sharp edge, the x-ray source size can be determined. [123,124,125] This method was used in Papers 3-5. Since the measurements were conducted at relatively low magnification, the calculated source sizes were verified with simulations using scalar wave theory (cf. Sect. 6.5), hence the impact of the detector blur and the partially coherent illumination was taken into account. For more details about the mathematics behind the edge spread method see, e.g., [126].

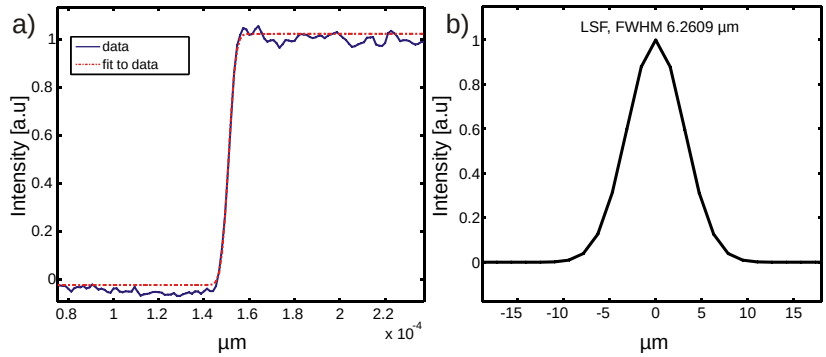

Figure 4.4. a) The intensity profile over a sharp 20 µm thick gold edge with a fitted function showed with a dashed curve. b) The LSF function with a FWHM of ~6 µm.

4.5.4 Modulation Measurements

By studying the modulation of periodic structures, quick estimates of the x-ray source size can be made making it possible to optimize the performance of the system by visual inspection. At first, a conventional mammography [127] resolution target was used, with the smallest features being 25 µm lines and spaces (20 LP/mm). With the improved electron beam focusing and a continuous decrease of the x-ray source size down to 4-5 µm, the need for smaller features became apparent and in 2007 custom-made resolution targets were manufactured using contact lithography. [128] The structures are based on ~10 µm high, gold electroplated features on 50 or 100 µm thick silicon substrates. Siemens stars, circular patterns and lines with varying periods from 30 µm to 6 µm (~166 LP/mm) are available for modulation measurements. Figure 4.5 shows an image taken during low power alignment of the gun with 3 µm lines and spaced resolved. This resolution target was used in Paper 6 for the source size measurements. The experimental modulation values were compared with wave-propagation simulations of the resolution target (cf. Sect. 6.5).

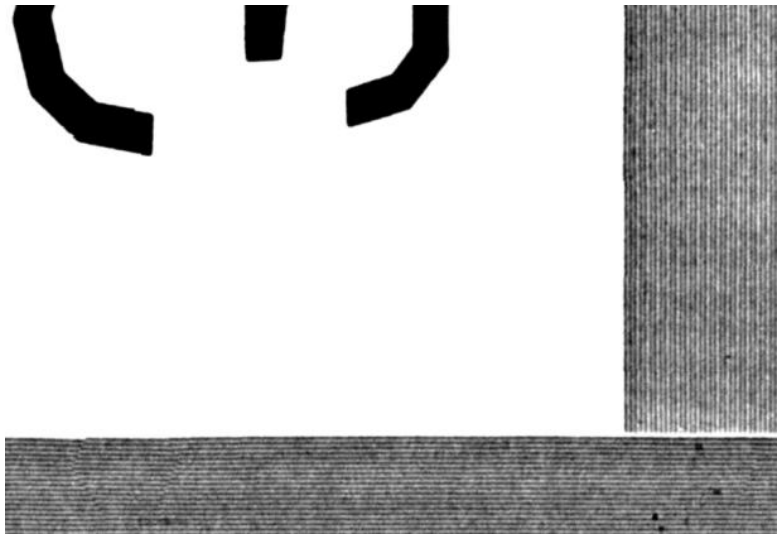

Figure 4.5. 3 μm gold lines clearly resolved. The gun was operated in low power (~4 W) microfocus mode for alignment and using a Mo target for x-ray generation.

4.6 Monte Carlo Analysis

The achievable image resolution and quality in x-ray projection imaging is directly proportional to the size and shape of the x-ray source. If the spatial distribution of the source is accurately known, the resulting x-ray image contrast and overall quality can be predicted. In order to understand how the e-beam intensity distribution affects the x-ray imaging properties of the system, the scattering of the electron beam interacting with the jet material has to be considered (see also Appendix A and Sect. 5.3).

Monte Carlo techniques are powerful numerical tools that can be used to predict the x-ray generating properties of materials with a high degree of accuracy. Software such as PENELOPE [129,130], CASINO [131-135] and NISTMonte [136] enable the numerical analysis of the x-ray generating properties of all known material combinations and the results generally compare well with experimental measurements. Both PENELOPE and CASINO have been extensively used to simulate the x-ray generation in liquid-jet targets.

The projection of x-ray generating volume in the jet is viewed in a 90 degree angle to both the jet and e-beam in the experimental arrangement; cf. Fig. 4.6, and the e-beam generated x-ray source can have different sizes in the horizontal, d_h and vertical, d_v direction due to anisotropic scattering.

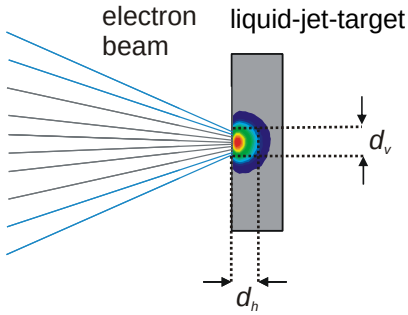

Figure 4.6. The x-ray source as seen from the object that is illuminated by the x-rays.

4.6.1 Simulated X-Ray Source Size

Figures 4.7 and 4.8 illustrate a CASINO simulation of a 1 μm (3σ) Gaussian e-beam hitting a Galinstan target, showing the absorbed energy (heat load) and the radial and longitudinal x-ray emission distribution (source size) in the material. Note that both distributions in Fig 4.8 are highly un-Gaussian, in particular the radial distribution which has a < 1 μm FWHM, but with long, low intensity tails extending to ~5 μm radially. However, the scattering at high-power operation is not trivial to determine using standard Monte Carlo techniques since the jet may be in a non-equilibrium state at the focus. The intense beam heats up the jet above the evaporation point resulting in density gradients that affect the scattering. Simulations show that the FWHM of the lateral scattering is hardly affected by a density reduction while the average penetration depth may increase substantially. As seen in Fig. 4.9, the penetration depth, and generated x-ray source size in the d_h direction, is highly dependent on the density of the material.

In summary; the x-ray source size in the vertical direction is thus mainly determined by the e-beam intensity distribution. In the horizontal direction, the x-ray source size is set by the penetration depth of the electron beam which is dependent on the anode material properties, its thermodynamic state and the electron beam energy.

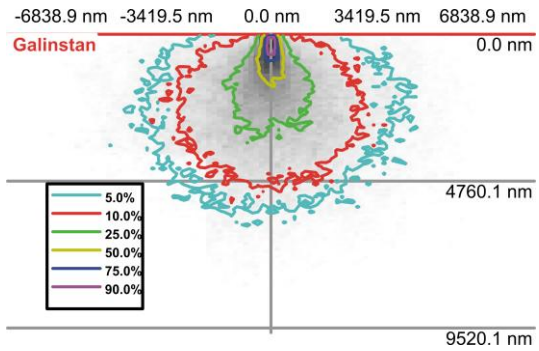

Figure 4.7. The absorbed energy in a Galinstan target showing energy contour lines (e-beam energy 50 keV).

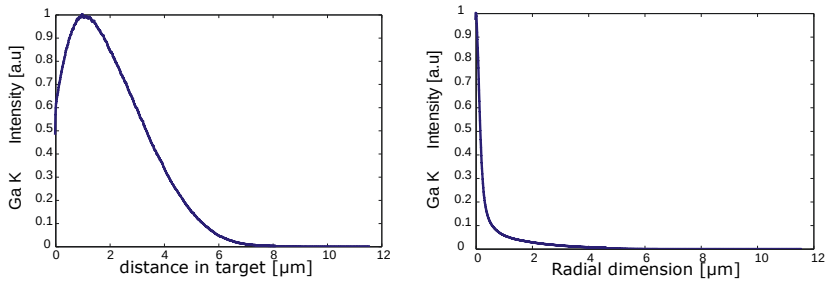

Figure 4.8. Monte Carlo simulated x-ray source sizes for Ga K_α radiation in the vertical (d_v) and horizontal (d_h) directions (e-beam energy 50 keV). Left: The Ga K_α line emission intensity in the direction of the e-beam travel. Right: The radial Ga K_α line emission intensity.

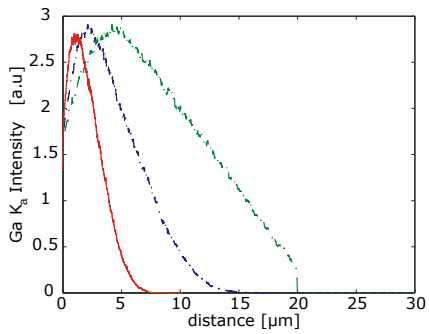

Figure 4.9. A Monte Carlo simulation of a reduced density Galinstan target. Density reductions of 0 (red), 50 % (blue) and 75 % (green) and 1 μm (3σ) Gaussian electron beam at 50 keV was assumed. The x-ray intensity distribution in the horizontal, d_h direction gets broader with reduced density.

4.6.2 Monte Carlo vs. Experimental Spectra

Figures 4.10 and 4.11 show quantitative spectra for tin, gallium, methanol and water jets using PENELOPE. Experimentally measured spectra from Papers 4-6 are included for comparison for the first three cases. The Monte Carlo simulations were made assuming a 5 μm FWHM Gaussian e-beam impinging on a cylinder, thus modeling an infinitely stable and fast jet. The agreement between the simulations and experimental data is excellent after correction for the measured x-ray source size for the metallic jets. The methanol simulation (Fig. 4.11, left panel) shows an expected spectral brightness that is a factor of 3-4 higher than what was measured, see also Paper 6. The discrepancy remains even after correction for the measured x-ray source. The reduced spectral brightness is now thought to be due to a combination of an aberrated e-beam focus and a very small diameter jet (~10 μm), leading to a substantial amount of e-beam power totally missing the jet, see Chapter 5 for a detailed discussion.

Figure 4.11 (right) depicts the simulated x-ray brightness of a 20 μm diameter water-jet based soft x-ray source. The e-beam parameters in the simulation were set to 40 keV beam energy with a 5 μm FWHM Gaussian spatial distribution. The spectral brightness of the O K_α line is 3.8×10^{11} [ph/(s·mA·μm²·sr·10eV BW), calculated with a source size of ~25 μm². The width of the O K_α line is ~1 eV [137], giving a line brightness of ~3.8×10^{12} [ph/(s·mA·μm²·sr·line),. These values should be compared with the values reported for laser-plasma produced (LPP) soft x-ray sources, having line brightness values in the range of ~4×10^{10} [138] Liquid-water-jets have previously been demonstrated in low power (~0.6 W) operation. [139] Solid, oxygen containing targets have also been proposed for soft x-ray generation via electron-impact. [140] In comparison to LPP sources, the main benefit of using an electron-impact based source for compact soft x-ray microscopy is the reduction in complexity and cost, gained from replacing the pulsed high-power laser. In addition, the absence of energetic ionic emission could increase the lifetime of the optics and merits thus further investigations.

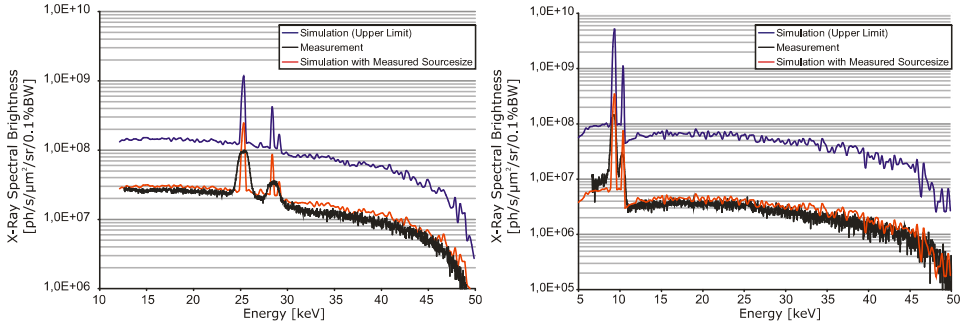

Figure 4.10. Metallic jet spectra. Left: Simulated (blue and red curves) and measured (black) liquid-Sn-jet spectrum. Right: Simulated (blue and red curves) and measured (black) liquid-Ga-jet spectrum. Adapted from [141].

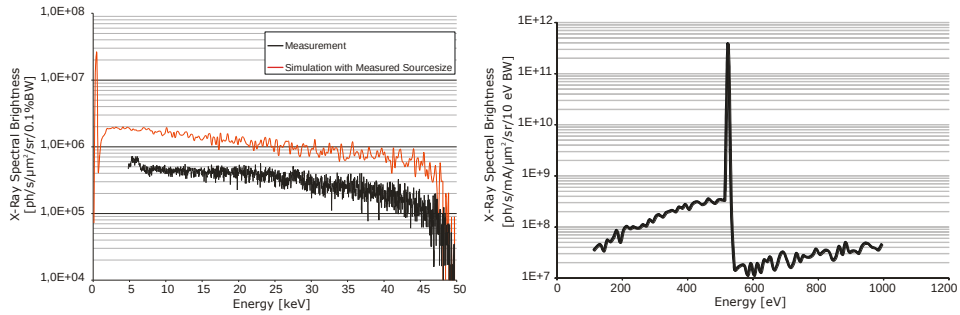

Figure 4.11. Non-metallic jet spectra**.** Left: Simulated (red curve) and measured (black) methanol spectrum. Adapted from [141] Right: Simulated spectrum for a water-jet target.

Chapter 5

Present Source Performance

In this chapter we investigate the present performance of the liquid-jet-target x-ray system using simulations with Lorentz2D-EM. The impact of aberrations on the e-beam focus intensity distribution and the consequences for x-ray imaging performance are studied.

5.1 Electron Gun Performance

The electron gun is based on the design that was used for the first proof-of-principle experiments. Its performance has gradually improved over time, mainly through upgrades of the cathode brightness. The original magnetic lens has been exchanged to a more powerful, short focal length lens, enabling more de-magnification of the source. Figure 5.1 shows a schematic drawing of the electron gun with its main components. The system consists of two basic parts, the acceleration gap in a diode configuration and an optical column with a magnetic lens for focusing. For the e-beam generation, a 50 μm diameter, carbon-guard-ring LaB_6 cathode is used.

The beam focusing is done using a single magnetic lens consisting of a heat treated ARMCO iron yoke and a coil with 1800 turns of copper wire. The target jet is placed just outside the magnetic lens at a distance of ~3.5 mm. Table 5.1 shows all of the relevant distances and system parameters for the gun including the spherical and chromatic aberration coefficients for the magnetic lens. The coefficients were calculated both by direct ray tracing using Lorentz2D-EM and by solving aberration integrals, with good agreement between the two methods. The geometrical de-magnification, $M = v/u$, is nominally ~0.09, leading to a ~4 μm focus if a 50 μm diameter cathode is used. The source can be further de-magnified by defocusing forces, such as the fields generated by the grounded anode hole or space charge.

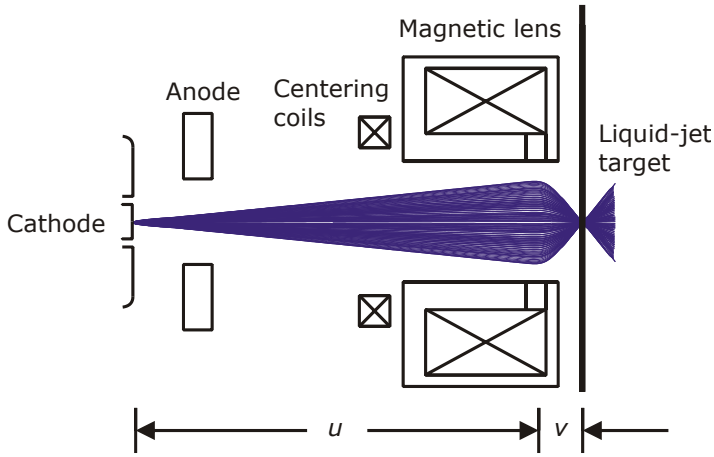

Figure 5.1. The electron gun and its optical column.

Parameter	Value
u	169 mm
v	14.5 mm
Focal length, *f*	13.9 mm (min.)
C_s at min. *f*	38 mm
C_c at min. *f*	13.9 mm
Beam Energy	50 keV (max)
Max. Beam Power at 1950 K (50 µm diam. LaB_6)	75 W
Calculated E-beam Brightness at 1950 K and 50 keV [A/cm^2/sr]	7.7×10^6

Table 5.1. A summary of the electron-gun parameters.

The maximum beam power for the 50 µm cathode with reasonable cathode lifetimes is ~75 W, but larger cathodes can generate substantially higher powers, with the maximum set by the 600 W high voltage power supply currently used. [142]

5.2 Simulation Results

The complete electron gun and its beam focusing properties were simulated using Lorentz2D-EM. The program is capable of solving all the relevant electrical and magnetic fields appearing in the gun using a boundary element method (BEM).

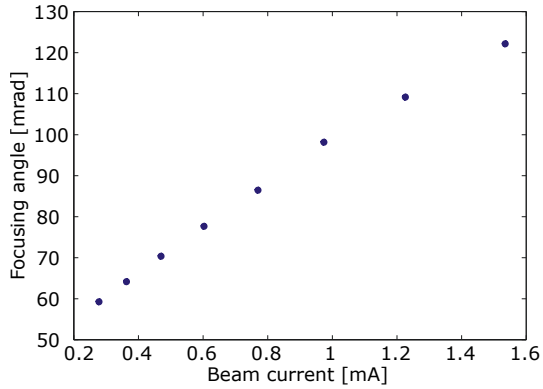

Figure 5.2. The simulated focusing angle as a function of beam current.

In order to fully analyze any magnetic saturation effects in the iron yoke for the magnetic lens, non-linear magnetization curves for the iron were implemented and analyzed using a combination of BEM and FEM techniques. The electron emission from the cathode can be simulated using accurate models for different emission regimes. The electrical fields are strong at the emitter surface and considerable field enhanced electron emission can occur. Hence, a Schottky emission model was used in the simulations. The impact of space charge on the ray trajectories was modeled using an iterative algorithm. By direct ray tracing in accurately solved fields, all the relevant electro-optical properties were found and data about the focus intensity profile could be extracted.

The e-beam system was therefore simulated for a range of beam currents in order to understand the system performance as a function of beam power. Figure 5.2 illustrates the focusing angle for a 50 keV beam as a function of the e-beam current. The focusing angle grows rapidly with increased beam current and already at ~20 W of beam power, aberrations start to affect the focusing quality, cf. Fig. 3.13 in Sect. 3.6.2.

Figure 5.3a shows the focus of the simulated beam in detail when calculated with 1.53 mA (~75 W) of beam current. The focus is heavily aberrated, with a distinct, large radius halo in the paraxial image plane. In addition, the depth of focus is relatively long (~500 μm) and it is not obvious at which plane the highest electron beam intensity or the best x-ray imaging performance is achieved. Figure 5.3b shows the location of the relevant beam cross-sections in detail. Figure 5.4 illustrates the simulated power density at different positions. The highest power density is not achieved at either the paraxial focus, where the FWHM of the high intensity peak is the smallest, or at the circle of least confusion, where all the rays

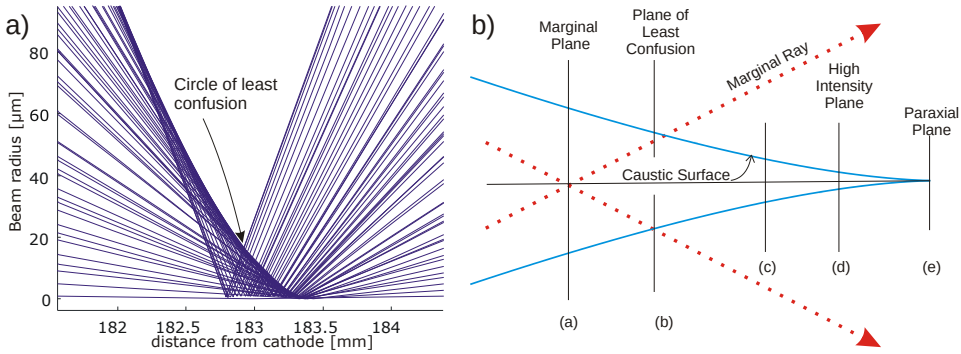

Figure 5.3. a) A simulated high power (~75 W) e-beam focus shown in detail. The circle of least confusion is ~18 µm in radius. b) The different regions in the focus area. Adapted from [143].

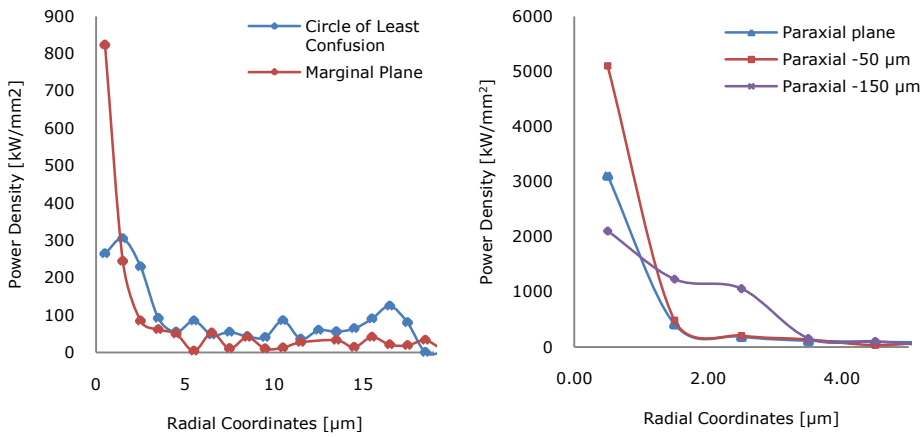

Figure 5.4. Intensity distributions in the focal area for a 50 keV ~75 W e-beam. Left: The e-beam intensity distribution at the circle of least confusion and marginal plane (regions (a) and (b) in Fig. 5.3b). Right: The e-beam intensity distributions near the paraxial plane (regions c, d and e in Fig. 5.3b).

are collected in the smallest radius. The peak power density is achieved at a location that is shifted 50 µm from the paraxial focus towards the circle of least confusion. In addition, the plane containing 50 % of beam power inside the smallest radius is located ~150 µm from the paraxial focus, see Fig. 5.5. The current to the magnetic lens can be experimentally controlled with a ~0.1 % precision which means that the beam can be shifted with an accuracy of ~15 µm. Thus, the whole e-beam depth of focus is accessible for experimental measurements.

There are a number of ways to control the spherical aberration in an electro-optical system. The aberration coefficients of the magnetic lens can be reduced by

optimization of the yoke geometry and the focusing performance can, thus, be slightly improved. By inserting a beam-radius limiting aperture in the beam path, the maximum convergence angle can be controlled.

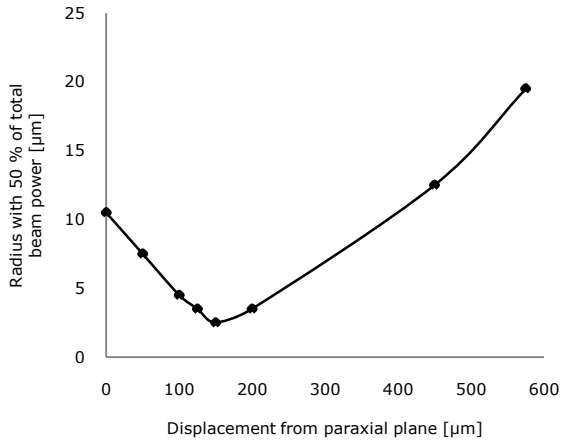

Figure 5.5. Intensity distribution in the focal area for a 50 keV ~75 W beam. The graph shows the radius containing 50 % of beam power as a function of displacement from the paraxial image plane.

However, this leads to a reduced beam current in the focus and reduced x-ray output and is, thus, not an alternative. A more appealing solution is the installation of another magnetic lens, which controls the beam radius and divergence entering the focusing lens. The goal is to obtain an e-beam focus that is constant in size in the whole usable power range.

5.3 X-Ray Performance

In this section we evaluate the x-ray imaging properties of the liquid-metal-jet x-ray source. As shown in Chapter 6, the spatial distribution of the x-ray spot defines the contrast and resolution in the image. Thus, in order to evaluate how the spherical aberration of the e-beam effects the x-ray imaging properties, the scattering of the electron beam interacting with the jet material has to be considered.

One way to understand the effect of electron scattering is by Monte Carlo simulations. By assuming a zero-radius electron-beam impinging on a material and calculating the shape and size of the generated x-ray volume, the x-ray response for a pencil e-beam can be determined. The total x-ray volume can then be found by a

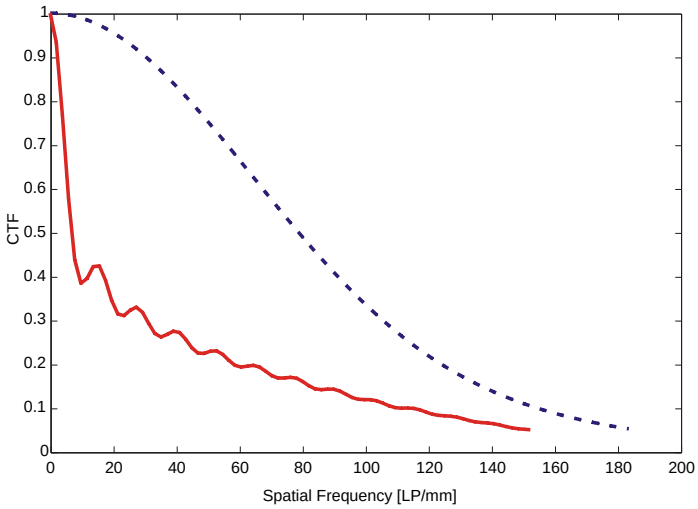

Figure 5.6. The CTFs for 5 W (dashed line) and 75 W (solid line) e-beams.

convolution of the pencil e-beam response with the incoming electron beam distribution, which can be simulated with high accuracy using methods from Sect. 3.7. The size and shape of the x-ray generated volume, in the observable 5-50 keV range, can thus be accurately determined for a low power case. The scattering is found to be small, with a FWHM of ~50-100 nm in the direction orthogonal to the electron-beam impact vector. The contribution to the total x-ray spot size in the vertical d_v direction (see Fig. 4.8) can thus be neglected to a good approximation. Thus, by taking the Fourier transform of the spatial intensity distribution of a simulated e-beam focus, the imaging properties of the x-ray source in the vertical direction can be determined. In Fig. 5.6, the solid line shows the calculated contrast transfer curve (CTF) in the vertical direction for an aberrated high power (75 W) e-beam focus. For comparison the low power case (5 W) is shown with the dashed line. The e-beam intensity distribution at the paraxial plane was used and the results would be somewhat different if distributions from other planes were used for the calculation. The overall trend is nevertheless clear. Spherical aberration is not affecting the cut-off frequency to a large degree, but gives a general reduction in contrast for a broad range of spatial frequencies.

In order to validate the simulated results, experimental modulation measurements using a Galinstan liquid-jet-target at different e-beam powers were used. The experimental data was measured at 100 LP/mm and Figure 5.7 shows the results. By calculating the CTF curves for the simulated beam focus in the power range

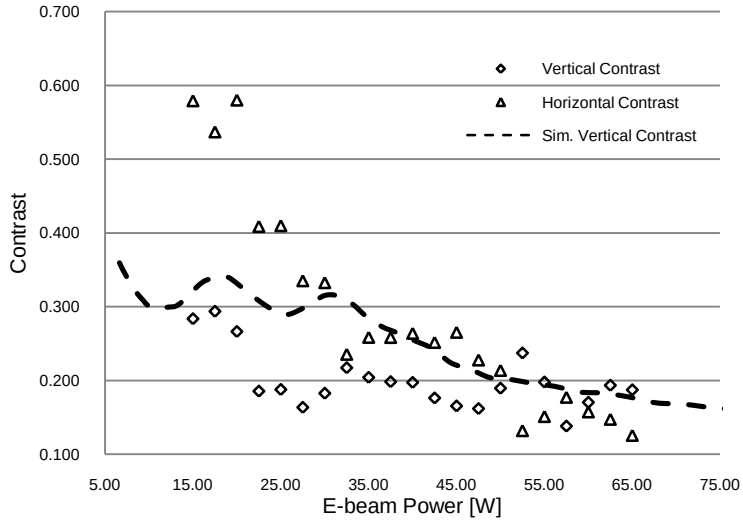

Figure 5.7. Left: Right: The simulated (- -) modulation of 100 LP/mm features as a function of beam power. The experimental contrast measurements are shown with (◊, vertical) and (△, horizontal).

used for the experiments, the expected modulation at 100 LP/mm in the image can be determined by multiplying the CTF's, properly scaled with the projected x-ray source size at the detector, with the Fourier transforms of the transmission function for the resolution target and the scaled detector PSF (cf. Sect. 6.5). The calculated modulation is shown as a dashed curve in Fig. 5.7, and is in good agreement with the measured modulation in the vertical direction. This confirms that the system is suffering from spherical aberration at high-power operation. The modulation in the horizontal, or in the direction of e-beam penetration into the jet, is also being reduced as a function power, albeit at a faster rate. This is thought to be due to the reduced density of the jet in the beam focus, although additional broadening caused by aberrations cannot be ruled out. Monte Carlo simulations indicate that a ~50 % average density reduction of the jet could explain the reduced modulation at the highest power.

5.4 Future Improvements

The x-ray source described above is based on a proof-of-principle arrangement with a single-lens electron gun and a gas-driven, non-circulating jet system and is not particularly suitable for advanced applications. In order to improve the

performance, reliability and accessibility further, a number of upgrades have to be implemented.

- The electron gun and its optical column have to be designed to allow aberration-free focusing in the full power range. Upgrading the optical column to a two-lens system will enable operation at the optimum focusing angle yielding constant e-beam focus size for a wide range of e-beam powers and energies. In addition, using line focusing of the electron beam, the x-ray brightness of the liquid-jet based source can be further increased.

- The jet propulsion system has to be upgraded to a closed-loop circulation system for comfortable operation. Larger and faster jets should allow for higher-power loads and reliability. By installing a suitable debris mitigation system, operation at much higher power densities than previously reported is enabled. The working distance from the x-ray source should be reduced to what is customarily found in conventional microfocus tubes, i.e., 10-30 mm.

The improvements mentioned above are presently implemented in a commercial prototype. Hundreds of hours of continuous liquid-jet operation and x-ray generation are already regularly achieved. More information about the jet x-ray source prototype is found at www.excillum.com.

Chapter 6

X-Ray Imaging

In this final chapter we study the impact of the increased x-ray brightness enabled by the liquid-jet target concept on conventional shadow projection x-ray imaging, the most common application area for x-rays. We start with a brief introduction to the importance of x-ray source brightness, and continue with absorption-based projection imaging and phase contrast imaging. The achievable resolution and contrast is discussed and some of the latest imaging results are presented.

6.1 X-ray Source Brightness

A small x-ray source provides sharp imaging. We have previously shown in this Thesis that small-spot x-ray sources are achievable with conventional e-beam technology. The spot size is only limited by the target material properties. In short, high-resolution imaging is always achievable. However, in order to obtain a reasonable exposure time or signal the x-ray flux has to be high. Thus, a high brightness source will generally increase the application performance by, i.e., increased resolution and/or improved exposure times. For instance, in medical radiography, where present exposure times often are short enough for practical purposes, an increase in x-ray brightness could be used to resolve smaller structures, which potentially leads to better diagnostics. In other applications, such as crystallography or phase-contrast imaging, the problem is often to acquire a useful signal within a reasonable exposure time. As it is increasingly difficult to maintain object or x-ray source stability over long periods of time, long exposure times generally lead to a decrease in image or signal quality. Increasing the source brightness at constant resolution will, thus, yield shorter exposure times. This is directly beneficial in applications where high throughput is important, such as non-destructive testing in the industry. Studies of fast processes at small length scales, such as single molecule diffraction studies, require extreme brightness values and fourth generation synchrotron facilities based on free electron lasing are being constructed for such high-end applications. [144]

Finally, since brightness is a quantity which does not say anything about the absolute values of the source size, flux or field divergence, but is rather a function of these factors, the suitability of particular source brightness for a certain application has to be understood. For instance, field emission cathodes can be used to create very small and bright x-ray sources, but at very low flux levels. This makes a practical implementation of an x-ray imaging setup where the object is large very difficult. The low flux is restricting the general size of the object under study to very small dimensions. This is required in order to get the object to a distance from the x-ray source where the geometrical magnification and signal on the detector is sufficient. In other words, high brightness has to be combined with an x-ray flux and a geometry that matches the signal requirements of the particular application.

6.2 Image Quality

An x-ray projection imaging arrangement consists of three basic components, namely the x-ray source, the object and the detector. Each of the components will affect the final image quality, which essentially can be summarized by four main performance characteristics.

i. *Spatial resolution*: The ability to distinguish adjacent high-contrast features. Spatial resolution in an x-ray projection image is generally limited by the x-ray source size and the detector resolution. For very small sources, diffraction can be the limiting factor.

ii. *Temporal resolution:* This determines the ability to capture structures in motion, a beating heart for instance, and is directly proportional to the x-ray flux impinging on the detector. If sub-micrometer resolution is needed at the same time, the x-ray brightness requirements will be extraordinarily high.

iii. *Contrast resolution*: The ability to differentiate a low-contrast feature from its background. The contrast is intimately connected with the material properties of the object under study. If the signal is strong enough and the dynamic range of the detector large, very small contrast difference can be detected. Contrast for objects can be increased by interference and diffraction effects although resolution can be affected.

iv. *Quantitative accuracy:* The ability to relate the image information to physically meaningful quantities in the object. This can be especially

challenging if the image has been distorted by polychromatic radiation, anisotropic magnification or interference effects.

6.3 Absorption Imaging

Figure 6.1 shows the basic x-ray imaging arrangement. The detector provides an image of the integrated absorption along each x-ray path. The detector records the intensity, *I*, which is proportional to the square of the time-averaged value of the electric field, E. This results in the following expression:

$$I = I_0 \exp(-2k\beta z), \tag{6.1}$$

where I_0 is the x-ray intensity before the object, $k = \frac{\omega}{c} = \frac{2\pi}{\lambda}$ the wavevector, β the imaginary part of the refractive index and z the object thickness. This imaging technique yields clear and informative images when there are distinct absorption differences between different parts of the object. However, there are a few quality-degrading effects that need to be understood and, as far as possible, controlled in order to be able to acquire a sharp absorption-contrast image.

One of the main factors that limit imaging performance is the projected size of the x-ray source, also known as penumbral blurring. As Fig. 6.1 shows, the radiation emitted from a source with size S, is projected through each point in the object, leading to a magnified source image of size SD/D_s at the detector. Even though the projected source size can be made small by reducing D, the detector will still limit the achievable resolution. The projected image of the sample is also magnified in projection geometry, with the magnification given by $1 + (D/D_s)$. However, the resolution in the magnified image cannot be better than the source size S.

X-rays generated in an electron-impact x-ray source will span a large energy range due to the continuous bremsstrahlung emission, (cf. Sect. A.2). Low-energy photons have a much lower transmission probability compared to the photons in the high-energy part of the spectrum. This can lead to a couple of unwanted side effects: virtually all of the photons of lower energies will be absorbed in a thick sample and, thus, not generate any image information. It only increases the radiation dose, which is especially important to avoid when imaging, e.g., patients in a hospital.

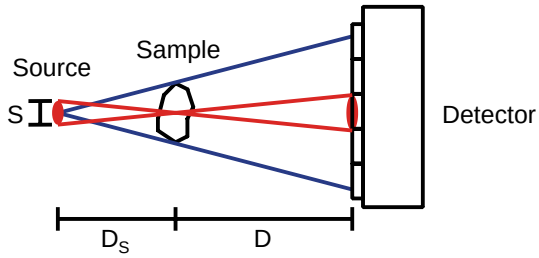

Figure 6.1. Sample magnification and source blur. Adapted from [145].

On the other hand, x-rays with too high energy will be absorbed to a very small extent and only increase the background signal on the detector and, consequently, lower the image contrast. The solution to this problem is energy filtering of the x-rays. Unfortunately, there are no really good x-ray filters, but a few millimeters of aluminum can be used to remove the low-energy photons. In the case of mammography, filters made of same material as the anode are used to make the spectrum more monochromatic around the Mo or Rh K_α and K_β peaks.

In addition to being absorbed, photons are scattered when interacting with matter, (cf. Sect. A.3.) The scattered radiation can cover the entire image area and will just increase the background signal level and, thus, decrease the contrast in the image. The two most important parameters influencing the amount of scattered radiation in the x-ray image are the irradiated field size and the thickness of the object. For radiographic examinations of thick bodies, such as the pelvis, the amount of scattered radiation can be as high as 90-95%. [146] A few common means for reducing the scattered radiation in medical radiography are compression of the object, increasing the distance from the object to the detector (which increases the exposure time), and the use of so-called radiation grids for absorption of x-rays striking the detector at too large angles (also increases exposure time). [147]

6.3.1 High Resolution X-Ray Imaging

The short wavelength of x-rays enables in theory resolution, orders of magnitude better what is achieved with visible light, to be achieved. For diffraction limited, incoherently illuminated optics, the resolution limit according to the Rayleigh criterion is given by $\delta = \frac{0.61\lambda}{NA}$. Microscopes operating with soft x-ray radiation (~250 eV - 5 keV), using Fresnel zone plates have been demonstrated with resolutions down to <15 nm using both compact and synchrotron sources. [148,149] However, for x-ray with energies above ~10 keV there is still a lack of

suitable optical elements for high resolution imaging. Lens-less microscopy techniques are therefore still almost exclusively used for x-ray imaging applications for hard x-ray energies.

X-ray microscopy can also be done in projection geometry. Significant advances were made by Cosslett and Nixon in the 50's with the use of high performance electron guns. Optimized magnetic electron lenses and thin foil targets allowed diffraction limited point-source x-ray imaging and resolutions down to ~100 nm were demonstrated. [150,151] Fresnel diffraction was considered only as a resolution limiting phenomena although images of biological samples taken at the time showed diffraction effects, which today would be considered as contrast enhancing. Later on modified electron microscopes were utilized for the purpose of producing even smaller x-ray sources suitable for projection microscopy. [152-155] Using volume-limited e-beam targets [156] and efficient detectors, resolution down to < 100 nm have been demonstrated in a projection geometry. [157]

6.4 Phase-Contrast Imaging

In all mainstream x-ray imaging modalities, the contrast mechanism has been based on attenuation. As a result, weakly absorbing samples are not imaged well and radiation dose has been a general concern. On the other hand, x-ray phase-contrast imaging relies on the refractive properties of structures, promising to have much better contrast at much lower dose. For x-rays, the real part of the refractive index for biological soft tissue is approximately 1.0 and in the range of 15–150 KeV, δ is about three orders of magnitude greater than β, (cf. Sect. A.4.) Thus, phase-contrast techniques shows promise to be significantly more sensitive than attenuation-based imaging. [158-161]

X-ray phase-contrast imaging has been a hot topic over the past decade. It is traditionally implemented via interferometry (crystal and grating based), diffractometry (analyzer-crystal based) and in-line holography (free-space propagation), as shown in Fig. 6.2. [162-165] Crystal based interferometry and diffractometry are practically restricted by the availability of high-brightness synchrotron facilities although some attempts have been made using compact sources. [166,167]

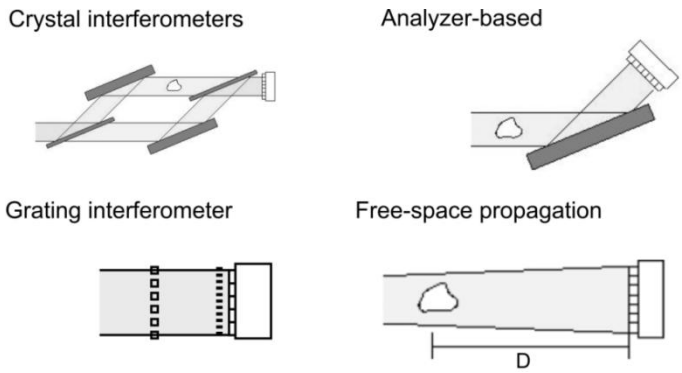

Figure 6.2. Experimental arrangements for different phase-contrast imaging techniques. Adapted from [145].

In 2006, Pfeiffer *et al.* reported on a major improvement for compact phase contrast imaging by implementing an imaging system based on a conventional large spot x-ray tube in combination with absorption gratings.[168,169] The method utilizes the Talbot effect generated by the grating structures.[170]

The in-line holography method, based on free-space propagation was proposed by Gabor in 1948. It was originally intended as a method to increase the resolution in aberration limited electron microscopes and he was awarded a Nobel Prize for the discovery in 1971. This imaging technique was early on demonstrated using both synchrotron radiation and compact sources. [171,172,173] Of particular importance for compact sources is the insensitivity of in-line holography to temporal coherence. However, the requirement of partial spatial coherence still places some demands on the x-ray source brightness. [174] A liquid-jet based microfocus system combined with improved detector technology can hopefully pave way for shorter exposure times and a wider utilization of compact sources for in-line phase-contrast imaging.

To conclude, phase-contrast imaging techniques also enable complementary information to be gathered from an image. This was earlier restricted to projected absorption data. The reconstruction of the phase distribution or δ, of an object is a theoretically and computationally challenging problem and the development of phase-contrast reconstruction algorithms is an area of intense research. [175-178]

6.5 Numerical Methods

The image forming process for x-rays can be analyzed with numerical methods. Below is a brief description of the methods used for the image simulations and source size measurements in Papers 3-6. The reader is referred to Refs 179 and 180 for more details. In order to accurately simulate the image forming process a number of parameters have to considered, namely; the properties of the wave front produced by the source, the object and the propagation of the wavefront from the object to the detector plane.

6.5.1 The Source

The simplest source to model is a monochromatic point source located at a distance from the illuminated object. A real source consists of many, statistically independent point sources which emit radiation with random phases and with a possibly wide range of energies. The coherence properties of the wavefront emitted from a chaotic and finite source can be studied rigorously using the Van-Cittert-Zernike theorem. [181] Fortunately, a partially coherent wavefront and its effect on an image can be modeled to a good approximation by convolving a scaled source intensity profile with a point-source image. Polychromatic sources can be modeled by integrating over the spectral distribution. [182,183]

6.5.2 Coherence

Coherence is the ability of a wave field to show interference. In coherent image formation the amplitude and phase of the wavefronts created in the interaction with an object have to be considered. This is in contrast to just adding intensities, which is the case for incoherent illumination. The condition of perfect coherence is only valid for monochromatic point source. The coherence properties of a wave field, in terms of x-ray source properties and measured at the object plane, can be related to two separable quantities namely, the longitudinal, l_l and lateral l_t, coherence lengths. [184] These are connected to the size and spectral emission properties of the source and can be expressed as

$$l_l = \frac{\lambda^2}{\Delta\lambda} = \frac{\hbar c}{\Delta \mathrm{E}_\gamma}, \tag{6.2}$$

where λ is the wavelength and $\Delta\lambda$ is the wavelength span emitted from the source and

$$l_t = \frac{z_{obj}\lambda}{S}, \tag{6.3}$$

where z_{obj} is the distance from the source to the object and S is the source size.

The longitudinal coherence length l_l represents the maximum path length difference that two rays can have and still exhibit interference. Features in an object that a separated by less that l_t can show strong interference effects. The lateral coherence length for a 5 μm diameter x-ray source located at 1 m from an object and with an average wavelength of 0.5 Å (~25 keV) is ~10 μm. Features separated with a distance less than can become hard to separate. Thus, in terms as of resolution, coherent illumination can be detrimental, which we will show in the next section.

6.5.3 Fresnel Zones

The intensity pattern generated by a monochromatic plane wave interfering with a point object consists of concentric rings with varying periodicity. The pattern produced is perfectly correlated with the shape needed to produce a diffractive optical element called a Fresnel zone plate.[185] In fact, the coherent image formation for a general thin object can formulated in terms of a superposition of Fresnel patterns. The radius of the *n*–th Fresnel zone can is defined as

$$r_n = \sqrt{n\lambda z}, \tag{6.4}$$

where z is the distance between the point object and the detector plane. The radius of the first zone $\sqrt{(\lambda z)}$ increases with the distance and will, in addition to the projected source size, limit the achievable resolution in projection based imaging. Figure 6.3 illustrates the phenomena.

6.5.4 The Object

A transmission function for the object can be defined by assuming that an object and its interaction with an x-ray wave-field can be fully described by the distribution of its complex refractive index. This is a very good approximation if the object is thin, i.e., there are no multiple-scattering events in the material, and is homogenous on atomic length-scales. Any periodicity on an atomic level will generate diffraction effects that cannot be accounted for using the refractive index. With the above mentioned limitations in mind the object can be defined by a function containing information about the complex refractive index n.

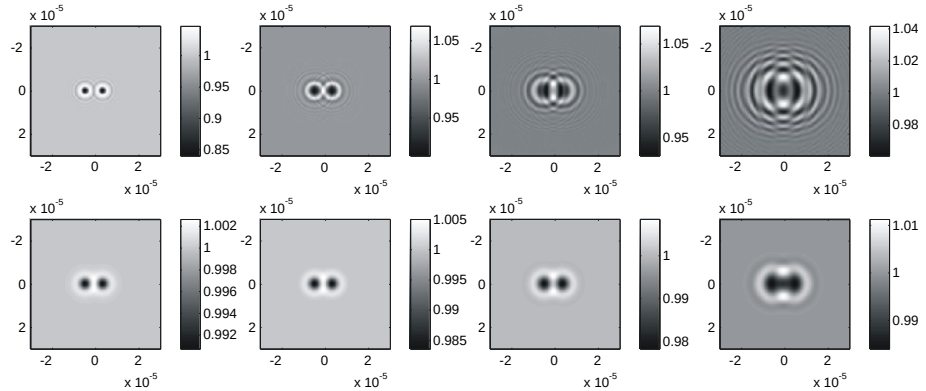

Figure 6.3. Effect of Fresnel diffraction on resolution. The figures show simulated images of two 3 μm diameter polystyrene (C_8H_8) spheres separated by 8 μm assuming monochromatic radiation at 25 keV at a distance r_1 from the source. The magnification, M, was constant at M=20. **Top row:** Intensity distribution on detector assuming point illumination and perfect detector. **Bottom row**: Intensity distribution after convolution with a 30 μm and 5 μm FWHM Gaussian detector and source. The spheres, even with the large separation, become harder to resolve as their first Fresnel zones start to overlap with increased r_1. The scale of the axes is in meters.

The transmission function of an object can be defined by

$$T(x, y, E) = exp(-ikn(x, y, E)t)\,, \tag{6.5}$$

where k is the angular wavenumber, $n(x, y, E)$ is the energy dependant complex refractive index distribution and t is the thickness of the object.

The field, E_1 , directly after the object can now be expressed as

$$E_1(x, y) = T(x, y, E)E_0(x, y), \tag{6.6}$$

where E_0 is the field impinging on the object. Note that $T(x, y, E)$ is a function of the x-ray energy and this has to be taken into account when simulating polychromatic sources.

6.5.5 Wave Propagation

The propagation of electromagnetic waves is described by Maxwell's equations. The scalar wave equation, neglecting polarization and considering only homogenous media, is expressed as

$$\nabla^2\psi - \frac{1}{c^2}\frac{\partial^2\psi}{\partial t^2} = 0, \tag{6.7}$$

where ψ is a scalar wave. By assuming monochromatic radiation, $\psi(x,y,t) = E_0(\mathrm{x,y})\exp(-i\omega t)$, the scalar wave equation can be simplified to the Helmholtz equation,

$$\nabla^2 E + k^2 E = 0, \tag{6.8}$$

where $k = \frac{\omega}{c} = \frac{2\pi}{\lambda}$ and $E(x,y) = E_0(x,y)\exp(ikz)$ is the time-independent wavefunction.

If the wavefront $E_1(x',y')$ directly after the object is known (cf. Eq. (6.6)), the field amplitude $E_2(x,y)$ at a distance z from the object can be calculated using the Fresnel-Kirchoff equation,

$$E_2(x,y) = \frac{1}{i\lambda}\iint \frac{E_1(x',y')e^{ikr}}{r}\cos\alpha\, dx'dy'. \tag{6.9}$$

Equation (6.9) basically says that the field amplitude at a point, $E_2(x,y)$, in the detector plane is a sum of all the spherical waves emitted from all of the points at the object plane (cf. Sect. 6.5.3). Using the paraxial approximation, Eq. (6.9) can be simplified and a propagator kernel can be defined [186,187]

$$H_z(x,y) = \frac{e^{ikz}}{i\lambda z}e^{\frac{ik}{2z}(x^2+y^2)}. \tag{6.10}$$

Since the field amplitude E_1 after the object is directly defined by Eq. (6.6), the intensity E_2 at the image plane can now be directly calculated by multiplication in Fourier space using

$$E_2 = \mathcal{F}^{-1}\big(\mathcal{F}(E_1)\times\mathcal{F}(H_z)\big), \tag{6.11}$$

where $\mathcal{F}$ is the Fourier transform and $\mathcal{F}^{-1}$ its inverse. The observable intensity is

$$I_{point} = |E_2|^2. \tag{6.12}$$

For spherical wave illumination, the propagation distance, z, in Eq. (6.10) should be scaled with the geometrical magnification, M, giving an effective propagation distance of $z_{eff} = z/M$. [188]

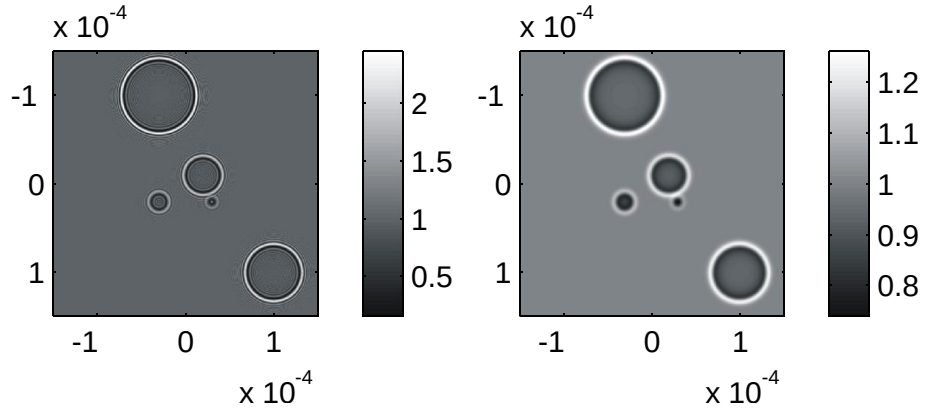

Figure 6.4. Left: Point source image. **Right:** Image calculation including source and detector blur assuming Gaussian distributions with FWHM of 5 and 30 μm, respectively. The scaling of the axes is in micrometers. **Simulation parameters:** Source-to-object distance, r_1=0.17 m, object-to-detector distance, r_2=1.02 m, M=7, δ =2.5e-6, β =2.3e-9. The scale of the axes is in meters.

Once the propagated point source intensity distribution, I_{point}, in a plane a distance z behind the object is known, the blurring caused by finite source size and detector resolution can be calculated by direct multiplication in Fourier space

$$I_{blurred} = \mathcal{F}^{-1}\Big(\mathcal{F}(I_{point}) \times \mathcal{F}(PSF_d) \times \mathcal{F}(PSF_s)\Big), \tag{6.13}$$

where PSF_d and PSF_s are the scaled detector and source intensity distributions, respectively. The scaling, calculated at the object plane, is $\frac{1}{M}$ for the detector and $(M-1)/M$ for the source. Figure 6.4 illustrates a numerical implementation of Eqs. (6.12) and (6.13), assuming monochromatic radiation at 10 keV and using polystyrene spheres as objects. The spheres range in size from 10 to 80 μm in diameter. Although the smallest can be considered a pure phase object, they are detected with good contrast due to Fresnel diffraction.

6.5.6 Source Size and Resolution Simulations

Simulations with the wavefront propagation techniques are valuable for understanding how partial coherence effects the source size measurements. As discussed in Sect. 4.5.1 and Sect. 5.3 the x-ray source size is an important parameter in itself and for determining the x-ray source brightness. Experimentally we determine the x-ray source size by measuring the image contrast of high-spatial frequency gratings. [128] The x-ray source sizes are typically in the range of 4-10

μm FWHM and grating structures with similar widths are used in the measurement. By iteratively comparing the experimental contrast measurements with the simulations assuming a Gaussian source, a Gauss-equivalent source size can be determined. The experimental source size measurements in Papers 3-6 were verified by such simulations. However, if the real x-ray source is highly non-Gaussian, i.e., for a heavily aberrated e-beam focus, the accuracy of the method is questionable. Better results can be obtained if the e-beam intensity profile is accurately known. The predictive ability of wavefront propagation techniques was tested in Sect. 5.3 where the resolution degradation induced by e-beam spherical aberration was confirmed with simulations.

Figure 6.5 illustrates a typical simulation for source size evaluation. In the simulations we assume a point source emitting monochromatic radiation at ~15.2 keV. This is the average x-ray energy for a pure Ga-jet target assuming a 50 keV electron beam. A transmission function was defined for the gratings consisting of 10 μm thick gold features on a 50 μm silicon substrate (δ_{Au}=1.32·10^{-5}, β_{Au}=1.93·10^{-6}, δ_{Si}=2.1·10^{-6} and β_{Si} =1.41·10^{-8}) and the wavefront was propagated to the detector plane. The point-source image was then convolved with scaled Gaussian source and detector distributions with PSF_{source}= 4 μm FWHM and $PSF_{detector}$= 31 μm FWHM, respectively. The image contrast was calculated by measuring the peak-to-peak intensities of the simulated gratings and dividing it with the object contrast which is ~0.9 at 15.2 keV.

The source-object distance in Fig. 6.5 is rather large (r_1=0.17 m) and the transverse coherence (l_t~3.5 μm) of the wavefront at the sample is significant and affects the resolution. The spatial coherence can be reduced by moving the sample closer to the source or by increasing the average x-ray energy of the source. Figure 6.6 shows the same simulation as in Fig. 6.5, but with a reduced distance to the source. The transverse coherence length l_t is now ~0.2 μm and the simulated contrast increases. In addition, the exposure time would be more than two orders of magnitude shorter due to the reduced distance to the detector.

Thus, a small source is not only giving enhanced contrast for weakly absorbing objects; it can also have negative effects on the resolution and contrast for strongly absorbing objects. [182] Experiments using solid Mo targets have shown that the resolution can be increased by coherence reduction. The increased resolution and contrast is partially due to the reduced electron penetration depth (higher Z and ρ), but also due to the higher average x-ray energy.

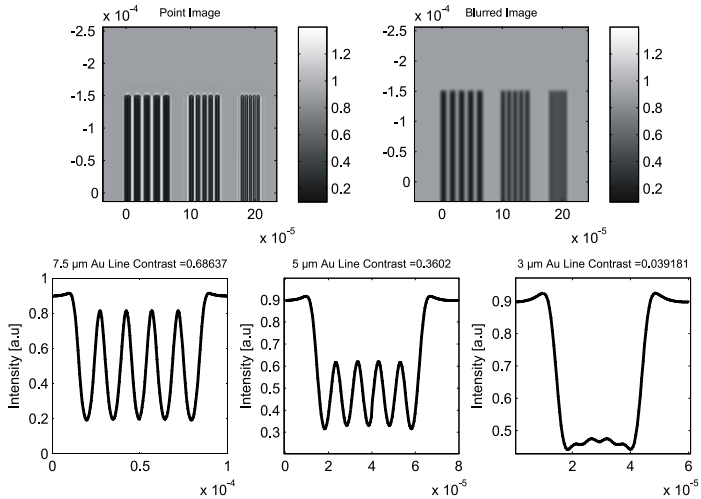

Figure 6.5. Effect of Fresnel diffraction on resolution and contrast. **Simulation parameters:** source-to-object distance, r_1=0.17 m, object-to-detector distance, r_2=1.02 m, M=7. **Top row: Left:** Simulated point source image of 7.5, 5 and 3 μm wide Au gratings. **Right:** Source and detector blurred image. **Bottom row:** Intensity profiles of the source and detector blurred Au gratings with the contrast displayed above the image. The scale of the axes is in meters.

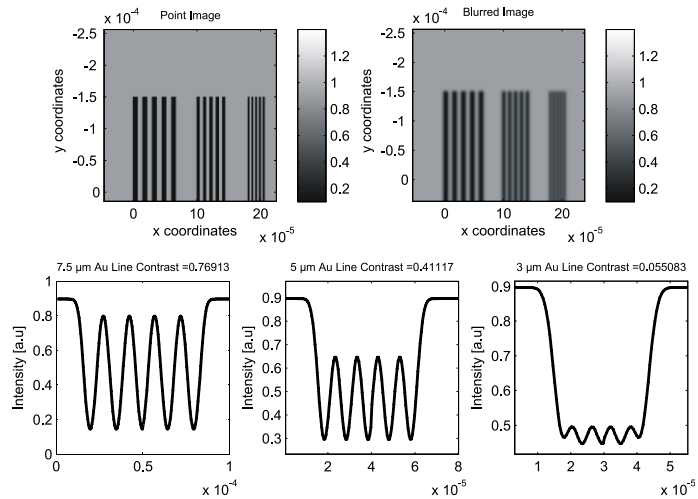

Figure 6.6. Effect of Fresnel diffraction on resolution and contrast. **Simulation parameters:** source-to-object distance, r_1=0.01 m, object-to-detector distance, r_2=0.06 m, M=7. **Top row: Left:** Simulated point source image of 7.5, 5 and 3 μm wide Au gratings. **Right:** Source and detector blurred image. **Bottom row:** Intensity profiles of the source and detector blurred Au gratings with the contrast displayed above the image. The scale of the axes is in meters.

6.6 Recent Experimental Results

Imaging, especially phase-contrast based, is a good test of the system stability and performance since any movement of the source during the exposure will degrade the image quality. Figure 6.7 depicts two typical images captured using a liquid-jet target for the x-ray generation. The contrast and resolution is good and shows that the liquid-jet target microfocus x-ray source is very suitable for phase contrast imaging of weakly absorbing objects. For details of the experimental conditions, see Papers 4 and 5.

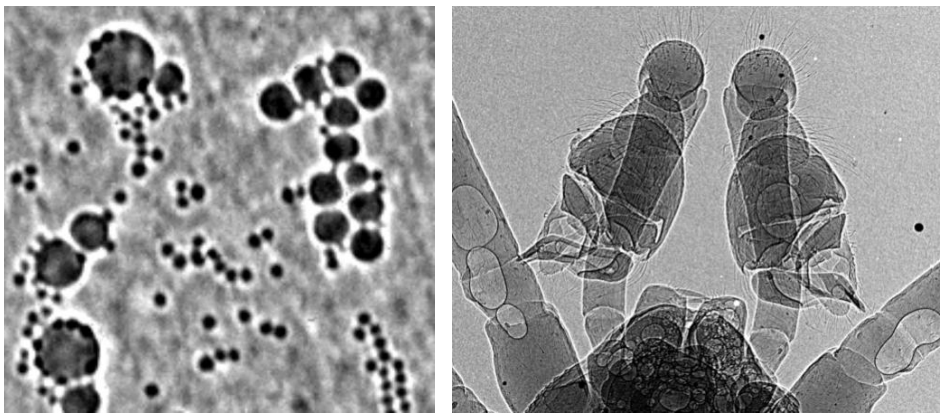

Figure 6.7. Phase-contrast imaging using a liquid-jet-target. Left: Image of polystyrene spheres with sizes ranging from 10-45 μm, showing extensive Fresnel diffraction at the edges. The smallest spheres are essentially pure phase objects. A Ga-jet was used as a target. Right: Image of a spider, showing enhanced edge contrast. <10 μm hairs on the pedipalps and head are clearly visible. A Sn-jet was used as an anode.

Appendix A

Basic X-ray Physics

In order to understand the mechanisms behind x-ray generation, an introduction to the basic physics behind electron-matter interactions is required. This Appendix gives the reader a brief outline of the topic. In addition to electron-matter interactions, the interaction of x-rays with matter is discussed and the complex refractive index is explained. For a more in-depth discussion of the phenomena described in this appendix, a number of standard text books are available, see, e.g., Refs 189-194

A.1 Electron-Matter Interaction

In addition to heat, a multitude of observable signals is created when electrons interact with materials. The signals can be classified as follows

i. X-rays emission, characteristic and bremsstrahlung
ii. Visible light emission, also known as cathodoluminescence
iii. Backscattered electrons
iv. Secondary electrons
v. Auger electrons

The only signal of interest for x-ray applications is the generated x-rays. However, the electron signals contain a lot of information about the target properties. Consequently they are routinely used in electron microscopy for material analysis. [195]

Backscattered electrons are generally considered a loss mechanism in x-ray tubes. In fact, they can actually generate image-quality-deteriorating, secondary x-ray sources if they by chance land in the field-of-view of the x-ray window. The fraction and energy of backscattered electrons (cf. Fig. A.1) is strongly dependant on the material composition and angle of incidence of the primary electron beam, with high Z materials and glancing angles generating the highest amount of backscattered electrons.

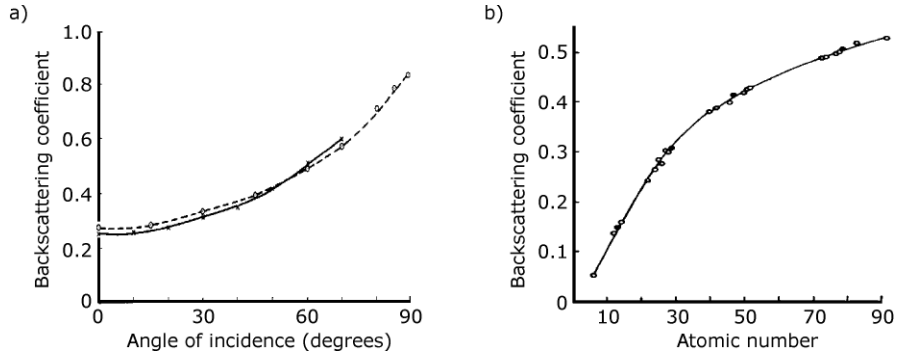

Figure A.1. Backscattering coefficient for 30 keV electrons as a function of a) angle of incidence, and b) atomic number of the target. Adapted from [196].

Secondary electrons are defined as the low-energy electrons generated at the surface of the material. Excellent resolution of the surface topology of materials can be gained by using them as the image-forming signal. Auger electrons are created in competition with characteristic x-rays and although they reduce the x-ray output, their energy is material specific and can be used to probe the material composition with good spatial resolution.

Considering the signal generated by (i-v) in terms of achievable spatial resolution in applications, the generated x-rays generally yield by far the lowest resolution; in particular for high energy x-rays which are not heavily attenuated by the material. The penetration depth and, thus, the size of the x-ray generating volume is extremely dependant on the energy of the primary electron beam and the material composition of the target. The minimum x-ray source size, set by the targets material properties is due to the fact that x-rays are generated in the whole interaction volume of the electron beam, which can be much larger than the size of the primary electron beam. Although secondary and Auger electrons are also produced throughout the interaction volume, they have very low energies and can only escape from a thin layer near the sample's surface and the observable secondary electron signal is, thus, coming from a ~nm depth below the surface giving outstanding resolution in electron microscopes. Similarly, soft x-rays, which are absorbed more easily than hard x-rays, will escape more readily from the surface of the interaction volume, see also Fig A.2.

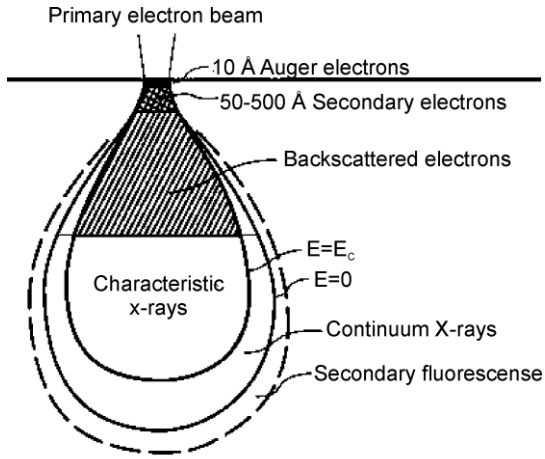

Figure A.2. The interaction volume in a material generated by electron scattering of the primary electron beam. Adapted from [197].

The size of the interaction volume is highly dependent on the electron beam energy and the material properties of the target and scales approximately as

$$Electron\ range \propto \frac{f_1(E)}{f_2(Z,\rho)}, \tag{A.1}$$

where E is the beam energy, Z the atomic number and ϱ the density. Note that the scaling is not linear and for detailed analysis of the electron-matter interactions and the signals produced, accurate Monte Carlo techniques (cf. Sect 4.6) are available.

A.2 X-Ray Generation

Here we first consider the Bremsstrahlung and later the characteristic x-rays. The total efficiency for generating continuum bremsstrahlung radiation from an e-beam interacting with a target is

$$\eta = KZV. \tag{A.2}$$

Here K is a material constant, typically set to 9.2 $\times 10^{-7}$ kV^{-1}, Z is the atomic number and V is the electron acceleration voltage. The general conclusion that can be drawn from Eq. A.2 is that for maximum x-ray conversion efficiency, high Z materials combined with high acceleration voltages should be used. This is often in conflict with Eq. A.1 which will determine the x-ray source size, with the consequence that small and high x-ray conversion efficiency sources are hard

produce by electron impact in bulk targets. Finally we note that the angular distribution of the continuum radiation is quite isotropic but gets more forward directed for high electron energies due to relativistic effects.

In addition to the continuum radiation, line or characteristic radiation is produced in electron-matter interactions. Line radiation is generated via ionization of bound inner shell electrons and yields material-specific and isotropic radiation. Green and Cosslett [198] found that the intensity of the K_α line radiation could be estimated using

$$N = N'\left(E_0 - E_{K_\alpha}\right)^{1.63}, \tag{A.3}$$

where N is the number of K_α photons generated per electron, N' is a material dependant constant, E_0 is electron beam energy and E_{K_α} is the energy required to ionize the K shell of the atom in question. Figure A.3 shows some experimental data for N'.

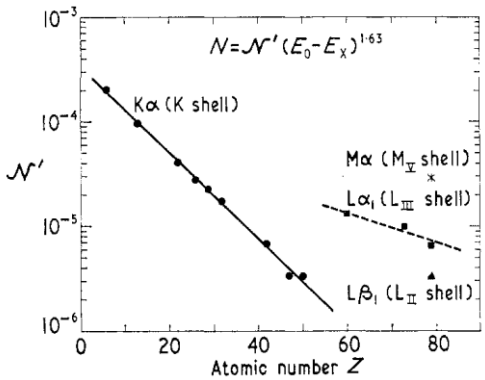

Figure A.3. Experimentally measured values for the efficiency coefficient N' as a function of the atomic number Z. Adapted from [198].

A.3 X-ray-Matter Interaction

In order to acquire a signal that can be analyzed, the x-rays have to interact with the object under study. When high energy photons (< 511 keV) penetrate through matter a number of things can occur, namely

i. *Photoelectric absorption*
ii. *Elastic scattering*
iii. *Non-elastic scattering*

The interactions most relevant for conventional, absorption-based projection x-ray imaging are the photoelectric absorption, which gives raise to the contrast in an x-ray image, and the non-elastic or Compton scattering which gives an unwanted background signal not contributing to the image formation. Elastic scattering is also known as coherent scattering and is closely connected to macroscopic refraction effects. Figure A.4 illustrates the interaction cross section as a function of energy for two materials.

A.4 Complex Index of Refraction

The complex refractive index describes the macroscopic phenomena of absorption and refraction for materials interacting with electromagnetic waves and can be expressed as

$$n = 1 - \delta + i\beta, \tag{A.4}$$

where δ describes refraction and β absorption. Note that both are generally very small positive numbers for x-rays. This is in contrast to the refractive index for materials illuminated by visible light, where the real part of n can be substantially larger than unity. This fact leads to a number of phenomena normally not experienced with visible light such as complete external reflection and that optics are generally very hard manufacture for use with x-rays due to the extremely low refractive powers of materials in the x-ray energy range.

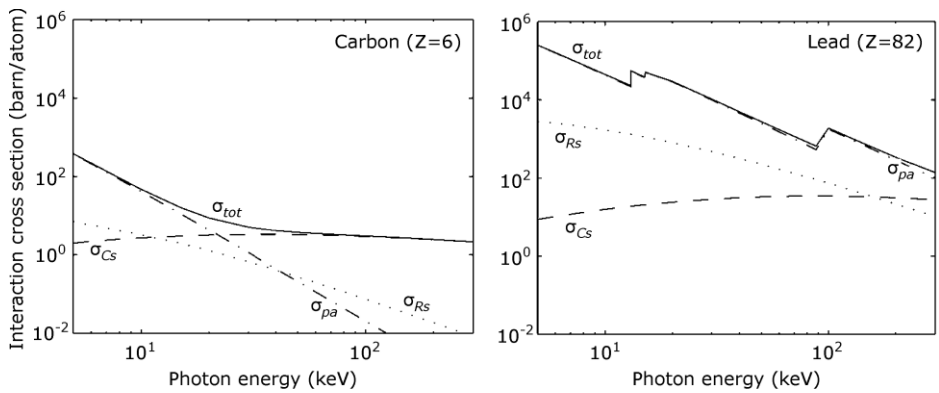

Figure A.4. The interaction cross section for some basic photon-matter interactions for carbon and lead in the energy range 5-300 keV. Subscript *pa* stands for photoelectric absorption, *Rs* for Rayleigh scattering, *Cs* for Compton scattering, and *tot* for the total cross section. Data generated by Ref. [200].

The index of refraction for a certain x-ray energy and material can be derived from the atomic scattering factors for small angle scattering, f_1^0 and f_2^0, which are related to the complex refractive index by

$$\delta(E) = 2\pi r_e(\hbar c)^2 1/E^2 \sum_a n_a f_{1,a}^0 \,, \tag{A.5}$$

$$\beta(E) = 2\pi r_e(\hbar c)^2 1/E^2 \sum_a n_a f_{2,a}^0, \tag{A.6}$$

where r_e is the classical electron radius, n_a is the number of atoms of type a per unit volume and the sum is over the different atomic species in the sample. The values for f_1^0 can be determined using absorption measurements of a material as a function of energy in combination with the Kramers-Kronig relations. The scattering factors can be found tabulated for all common elements and broad energy ranges, see, e.g., Refs 199 and 200.

Summary of Papers

This Thesis is based on six Papers. He is the main author for Papers 1, 4, and 6. In all of the six papers the author was actively involved in the planning, preparation and the execution of the experiments. His particular interest has been the electron gun. The author was not responsible for the data analysis and fluid mechanical calculations in paper 2.

Paper 1 presented the status of the high-brightness liquid-jet based x-ray source in 2004. Early calculations and simulations on the electron gun performance were made. The simulations and calculations indicated that the electron gun brightness could be substantially increased.

Paper 2 investigates the fluid mechanics of microscopic high-speed liquid-metal-jets in vacuum by dynamic-similarity experiments using water. It is concluded that a 30-μm diameter, 500-m/s liquid-tin jet in vacuum should be possible to generate.

Paper 3 describes the debris generation that can occur at high power operation for metal-jet targets. Debris rates are quantified as a function of system parameters, namely; jet speed and size and the applied e-beam power. Debris rates are found to be growing exponentially with deposited power.

Paper 4 reports on the first phase-contrast imaging results using the liquid-jet-target x-ray source. Good resolution and short exposure times are demonstrated using two model samples, a spider and polystyrene spheres.

Paper 5 reports on the performance of a low temperature gallium-jet target x-ray source with characteristic K_α emission at 9.2 keV. The x-ray source is characterized in terms of spectral brightness. Possible applications such a crystallography and microscopy are discussed.

Paper 6 presents the first non-metal-jet x-ray source operating at high power. We show that methanol jets can be operated stably up to the complete evaporation of the target. This first proof-of-principle experiment opens up the possibility of using all compounds and elements for x-ray generation. Soft x-ray generation at high brightness levels using water jets is proposed.

Acknowledgments

This Thesis would not have been possible without contributions from several people. I would like to thank them for their help and for creating a nice working atmosphere.

First of all, my supervisor Hans Hertz. His enthusiasm, his encouragement, and the trust in me to choose my own directions in the project has been the driving force for success and, most importantly, made this journey a most pleasant and educating experience.

My closest colleagues during these years: Mikael Otendal for all the tough times spent together in the lab and for having patience with my sometimes wild ideas. Oscar Hemberg for introducing me into the fascinating world of electron guns and optics.

All present and former members of the Biomedical and X-Ray Physics group that haven't been mentioned earlier. Magnus Lindblom, Ander Holmberg, Johannes Ewald, Moritz Schlie, Peter Skoglund, Richard Tjörnhammar, Olov von Hofsten, Mikael Bertilson, Per Takman, Klaus Biedermann, Kjell Carlsson, Anna Gustrin, Linda Lundström, Jessica Hultström, Robert Rosén, Göran Manneberg, Otto Manneberg, Karolina Pihlblad, Elle Kristiansson, Peter Unsbo, Martin Wiklund, Nils Åslund, Agnès Sauleda Brossa, Mats Gustafsson, Björn Hansson, Jalmar Thoresen, Anders Liljeborg, and Milan Pokorny.

Special thanks to José M Fernandez-Varea for introducing Monte Carlo techniques into our work. Thanks go also to Rolf Helg and Kjell Hammarström for their superb skills in the mechanical workshop. None of the experimental results would have been possible without their help.

Finally, my family, for love and understanding.

Bibliography

[1] R. B. Bergmann, F. T. Bessler and W. Bauer, *Non-Destructive Testing in the Automative Supply Industry –Requirements, Trends and Examples Using X-Ray CT*, ECNDT, (2006).

[2] J. Als-Nielsen and D. McMrrow, Chapter 4 – Kinematical Diffraction, pp 107-172 in [190].

[3] M. V. Klein, T. E. Furtak, Optics, (John Wiley & Sons, New York, 1986), Chapter 4.2 - Radiometry and Photometry, pp 203-222.

[4] H. Winick, *Synchrotron Radiation Sources – Present Capabilities and Future Directions,* J. Synchrotron Rad. **5**, 168 (1998).

[5] O. Hemberg, M. Otendal and H. M. Hertz, *Liquid-metal-jet anode electron-impact X-ray source*, Appl. Phys. Lett. **83**, 1483 (2003).

[6] O. Hemberg, M. Otendal, and H.M. Hertz, *A liquid-metal-jet anode x-ray tube*, Opt. Engin. **43**, 1682 (2004).

[7] X-ray tube, from Wikipedia, see http://en.wikipedia.org/wiki/X-ray_tube (11 May 2008).

[8] Kimball Physics Inc. Manual EGG-4200 / EGPS-4200 electron gun and power supply system (2007).

[9] H. J. Quiesser, ed, X-Ray Optics – Applications to Solids, (Springer-Verlag, Berlin, 1977), Chapter 2 - High Brilliance X-Ray Sources, pp 9-32.

[10] J. Freudenberg *Perspectives on Medical X-Ray Imaging*, Nucl. Instrum. Methods Phys. Res. A **466**, 99 (2001).

[11] R. K. Smither, G. S. Knapp, E. M. Westbrook, and G. A. Forster, "High Intensity X-Ray Source Using Liquid Gallium Target", US Patent 4,953,191 (1989).

[12] M. Schuster, "X-Ray Generator", US Patent 5,052,034 (1990).

[13] G. Harding, A. Thran, and B. David, "Liquid Metal Anode X-Ray Tubes and the Potential for High Continuous Power Operation", Radiat. Phys. Chem. **67**, 7-14 (2003).

[14] B. David, H. Barschdorf, V. Doormann, R. Eckart, G. Harding, J-P. Schlomka, A. Thran, P. Bachmann, and P. Flisikowski, *Liquid Metal Anode X-Ray Tube*, Proc. SPIE. **5196**, 432 (2003).

[15] M. Sedlaček, Electron Physics of Vacuum and Gaseous Devices (John Wiley & New York, 1996).

[16] A. Chao and M. Tigner, ed, Handbook of Accelerator Physics and Engineering (World Scientific, Singapore, 2002).

[17] R. Bakish, Introduction to Electron Beam Technology, (John Wiley & Sons, New York, 1962).

[18] S. Humpries, Jr. Charged Particle Beams (John Wiley & Sons, New York, 1990).

[19] S. Humpries, Jr. Principles of Charged Particle Acceleration (John Wiley & Sons, York, 1996).

[20] J. Orloff, ed, Handbook of Charged Particle Optics (CRC Press, New York, 1997).

[21] A. Septier, ed., Focusing of Charged Particle - Volume I (Academic Press, New York, 1967).

[22] A. Septier, ed., Focusing of Charged Particle - Volume II (Academic Press, New York, 1967).

[23] A. Septier, ed., Applied Charged Particle Optics Part C: Very-High-Density Beams (Academic Press, New York, 1983).

[24] P. W. Hawkes and E. Kasper, Principles of Electron Optics, Volume 1: Basic Geometrical Optics (Academic Press, New York, 1996).

[25] P. W. Hawkes and E. Kasper, Principles of Electron Optics, Volume 2: Applied Geometrical Optics (Academic Press, New York, 1989).

[26] O. Klemperer, Electron Optics (Cambridge University Press, 1971).

[27] J. Orloff, ed, Chapter 1- Computational Techniques for Design of Charged Particle Optical Systems, pp1-76, in [20].

[28] T. Koch, *Design and Evaluation of a Particle Acceleration Simulation Package*, Master Thesis (Royal Institute of Technology, Stockholm 2003).

[29] M. Sedlaček, Chapter 2.2.1 – Thermionic Emission, pp 61-69, in [15].

[30] J. Orloff, ed, Chapter 2 – A Review of the Zr/O Schottky Cathode, pp 77-103, in [20].

[31] P. W. Hawkes and E. Kasper, Chapter 44.5 – Field Electron Emission, pp 927-933, in [25].

[32] J. Orloff, *Survey of electron sources for high-resolution microscopy*, Ultramicroscopy **28**, 88 (1989).

[33] SPIE Handbook, Volume 1: Microlithography, Section 2.5.4, available online at http://www.cnf.cornell.edu/cnf_spie54.html.

[34] Hamamatsu microfocus transmission target x-ray tube, L8321-01, see e.g., http://sales.hamamatsu.com/assets/pdf/parts_L/L8321-01_TLSO1046E03.pdf.

[35] K. Togawa, H. Baba, K. Onoe, T. Inagaki, T. Shintake, H. Matsumoto, *CeB6 electron gun for the soft X-ray FEL project at SPring-8*, Nucl. Instrum. Methods. Phys. Res. Sect. A **528**, 312 (2004).

[36] W. A. Mackie, K. J. Kagarice, C. L. Fast, *Development of a (100) Hafnium Carbide Thermionic Electron Source with Built-in Guard Ring and Heater,* Vacuum Electronics Conference, b IEEE International , 201-202, (2006).

[37] K. Togawa, T. Shintake, T. Inagaki, K. Onoe, T. Tanaka, H. Baba, and H. Matsumoto, *CeB_6 electron gun for low-emittance injector*, Phys. Rev. ST. Accel. Beams. **10**, 020703 (2007).

[38] V. Katsap , "High Brightness Thermionic Cathode", US Patent 7,176,610.

[39] A. Broers, S. Xia, C. Maloney, X. Zhu, and E. Munro, *High brightness limited area cathodes*, J. Vac. Sci. Technol. B. **9**, 2929 (1991).

[40] C.E. Maloney, H. Nakamura, A.N. Broers, S. Xia and L. Peters, *Realization of Limited-Area Cathodes and their Performance in an Electron Optical Column,* J. Vac. Sci. Technol. B. **12**, 26 (1994).

[41] E. Munro X. Zhu, J. Rouse and V. Katsap, *Non-flat and limited-area cathodes emission modeling*, 2007 8th IEEE International Vacuum Electronics Conference, 179-80 (2007).

[42] LaB6-01 Technical Bulletin, Kimball Physics, available at http://www.kimphys.com/cathode/support_PDF/LaB6_01B.pdf..

[43] M. Sedlaček, Chapter 2.2.1 – Thermionic Emission, pp 61-69, in [15].

[44] A. Chao and M. Tigner, Sect. 2.4.2.1 - Gun characteristics, pp 101-102 in [16].

[45] A. Broers, S. Xia, C. Maloney, X. Zhu, and E. Munro, *High brightness limited area cathodes*, J. Vac. Sci. Technol. B **9**, 2929 (1991).

[46] F. Sannibale, Fundamental Accelerator Theory, Lecture No. 9, Particle Sources, lecture notes available online at http://controls.als.lbl.gov/als_physics/Fernando/USPASJun07Lectures/L11_ParticleSources.pdf (May 2008).

[47] J. P. Vermeulen, New developments in FESEM Technology, Carl Zeiss SMT, see e.g., http://www.smt.zeiss.com/nts.

[48] M. Sedlaček, Chapter 8.6 - Linear Accelerators, pp 365-384, in [15].

[49] A. Septier, ed., Chapter 2.1, pp 233-236 in [21].

[50] V. E Cosslett, *Intensity limitations in a point source of X-rays*, Proc. Phys. Soc. **65,** 782 (1952)

[51] LaB_6 Surface Recession vs Theoretical Brightness, technical note available at http://www.kimphys.com/cathode/cath_tech.htm.

[52] M. Sedlaček, Appendix B, pp 473-474, in [15].

[53] S. Humpries, Jr, Chapter 2.4 – Conservation of Phase-Space Volume, pp 36-49, in [18].

[54] P. W. Hawkes and E. Kasper, Chapter 47 – Brightness, pp 972-988, in [25].

[55] P. W. Hawkes and E. Kasper, Chapter 48 – Emittance, pp 989-1003, in [25].

[56] S. Humphries, Jr, Chapter 3 – Introduction to Beam Emittance, pp 79-132, in [18].

[57] K Togawa, RIKEN SPring-8 Center Japan, Personal Communication.

[58] J. Orloff, ed, Chapter 7 – Space Charge and Statistical Coulomb Effects, pp 275-318 in [20].

[59] J. Orloff, ed, Chapter 7.3.5 – Space Displacement Distribution in the Extended Two-Particle Approximation, pp 293-302 in [20].

[60] P. W. Hawkes and E. Kasper, Chapter 49 – The Boersch Effect, pp 1004-1016, in [25].

[61] M. Sedlaček, Chapter 1.3.1 - Equations of Motion, pp 25-29, in [15].

[62] J. Rouse and E. Munro, *Three-dimensional computer modeling of electrostatic and magnetic electron optical components*, J. Vac. Sci. Technol. B. **7**, 1891 (1989).

[63] X. Zhu and E. Munro, *A computer program for electron gun design using second-order finite elements*, J. Vac. Sci. Technol. B. **7**, 1862 (1989).

[64] E. Munro, *Numerical modeling of electron and ion optics on personal computers*, J. Vac. Sci. Technol. B. **8**, 1657 (1990).

[65] E. Munro, *Computational modeling techniques in charged-particle optics*, Proc. SPIE **2014**, 2 (1993).

[66] J. Rouse, X. Zhu and E. Munro, *Solution of Electron Optics Problems with Space Charge in 2D and 3D*, Proc. SPIE **2522**, 375 (1995).

[67] T. Mulvey, *The Magnetic Circuit in Electron Microscope Lenses,* Proc. Phys. Soc. B, **66**,441 (1953).

[68] S. Humphries, S. Russell, B. Carlsten, L. Earley, and P. Ferguson, *Circular-to-planar transformations of high-perveance electron beams by asymmetric solenoid lenses*, Phys. Rev. ST Accel. Beams **7**, 060401 (2004).

[69] S. J. Russell, Z.-F. Wang, W. B. Haynes, R. M. Wheat, B. E. Carlsten, L. M. Earley, S. Humphries, and P. Ferguson, *First observation of elliptical sheet beam formation with an asymmetric solenoid lens,* Phys. Rev. ST Accel. Beams **8,** 080401 (2005).

[70] J. Orloff, ed, Chapter 4- Magnetic Lenses for Electron Microscopy, pp 143-177, in [20].

[71] J. Orloff, ed, Chapter 5.2.6- Aberrations of Electrostatic lenses, pp 191-192, in [20].

[72] J. Orloff, ed, Chapter 5- Electrostatic lenses, pp 177-223 in [20].

[73] U. W. Arndt, J. V. P. Long and P. Duncumb, *A Microfocus X-ray Tube Used with Focusing Collimators,* J. Appl. Cryst. **31**, 936 (1998).

[74] Phoenix x-ray microfocus x-ray tubes; more info available online at http://www.phoenix-xray.com

[75] J. Orloff, ed, Chapter 5 –Aberrations, pp 223-275 in [20].

[76] A. V. Crewe, *Optimization of Small Electron Probes,* Ultramicroscopy **23**, 159 (1987).

[77] G. M. Gallatin, *Analytical Evaluation of the Intensity Point Spread Function,* J. Vac. Sci. Technol. B **18,** 3023 (2000).

[78] B. Rafferty, T. R. Groves, *Wave optical Calculations of Electron Probes*, J. Vac, Sci. Technol. B **19**, 2607 (2001).

[79] J. Orloff, ed, Chapter 8 –Resolution, pp 319-361 in [20].

[80] M. Sato, J. Orloff, *A new Concept of Theoretical Resolution of an Optical System, Comparison with Experiment and Optimum Condition for a Point Source*, Ultramicroscopy **41**, 182 (1992).

[81] J. Orloff, *High Resolution Focused Ion Beams,* Rev. Sci. Instrum. **64**, 1105 (1993).

[82] G. Liebmann and E. M. Grad, *Imaging Properties of a Series of Magnetic Electron Lenses, Proc. Phys. Soc.* **64,** 956 (1951).

[83] M. E. Haine, The Electron Microscope (Spon, 1961).

[84] T. Mulvey and M. J. Wallington, *Electron lenses*, Rep. Prog. Phys. **36**, 347 (1973).

[85] E. Munro, X. Zhu, J. Rouse and H. Liu, *Aberration Analysis of Wide-Angle Deflectors and Lenses by Direct Ray-Tracing, and Comparison with Conventional Aberration Theories*, Proc. SPIE **2522,** 54, (1995).

[86] H. C. Chu and E. Munro, *Computerized optimization of electron-beam lithography systems*, J. Vac. Sci. Technol. **19**, 1053 (1981).

[87] O. Scherzer, *Über einige Fehler von Elektronenlinsen,* Z. Physik **101**, 593 (1936).

[88] O. Scherzer, *The Theoretical Resolution Limit of the Electron Microscope*, J. Appl. Phys. **20**, 20 (1949).

[89] P. E. Batson, N. Dellby, O. L. Krivanek, *Sub-Ångstrom Resolution using Aberration Corrected Electron Optics*, Nature **418**, 617 (2002).

[90] D. J. Smith, *Development of Aberration-Corrected Electron Microscopy*, Microsc. Microanal. **14**, 2 (2008).

[91] P. W. Hawkes and E. Kasper, Part II -Calculation of Static Fields, pp 61-194 in [24]

[92] M. Sedlaček, Chapter 1.2 –Numerical Methods, pp 7-25 in [15]

[93] A. Septier, ed, Chapter 1.2 –Numerical Solution of Laplace's and Poisson's Equation and the Calculation of Electron Trajectories and Electron Beams, pp 45-99 in [21]

[94] H. Ahmed and E. Munro, *Optimization of the Performance of High-Brightness Electron Guns*, J. Vac. Sci. Technol. **10**, 972 (1973).

[95] E. Munro, *Design and optimization of magnetic lenses and deflection systems for electron beams*, J. Vac. Sci. Technol. **12**, 1146 (1975).

[96] H. C. Chu and E. Munro, *Computerized optimization of electron-beam lithography systems*, J. Vac. Sci. Technol. **19**, 1053 (1981).

[97] E. Munro, J. Rouse, H. Liu, L. Wang and X. Zhu, *Simulation Software for Designing Electron and Ion Beam Equipment*, Microel. Eng. **83,** 994-1002 (2006).

[98] Lorentz2D-EM, v.6.4, www.integratedsoft.com.

[99] S. Humpries, Jr, Chapter 7 – Calculation of Particle Orbits in Focusing Fields, pp 137-165, in [19].

[100] A.Chao and M. Tigner, ed, Chapter 2.4.2.3 –Radial Dynamics, pp 102-103 in [16].

[101] M. Sedlaček, Chapter 6.3.1 –Beam spreading, pp 236-240 in [15].

[102] J. Orloff, ed, Chapter 6.5 –Direct Ray-Tracing of Aberrations in Combined Lens and Deflection systems, pp 36-47 in [20].

[103] J. Orloff, ed, Chapter 3.1 –Polepiece Analysis by FOFEM, pp 13-15 in [20].

[104] V. E. Cosslett, *Intensity Limitations in a Point Source of X-Rays*, Proc. Phys. Soc.Sect. B **65**, 10 (1952).

[105] A. Mueller, *On the Input Limit of an X-Ray Tube with Circular Focus*, Proc. R. Soc. A **117,** 30 (1927).

[106] W. Ehrenberg and W. E. Spear, *An Electrostatic Focusing System and its Application to a Fine Focus X-Ray Tube***,** Proc. Phys. Soc. **64,** 67 (1951).

[107] D. E. Grider, A. Wright and P. K. Ausburn, *Electron Beam Melting in Microfocus X-Ray Tubes***,** J. Phys. D: Appl. Phys. **19**, 2281 (1986).

[108] Open type jet-anode microfocus x-ray source, commercial prototype, more information available online at www.excillum.com.

[109] B. Verman, L. Jiang and B. Kim, *Microfocusing Source and Multilayer Optics Based X-ray Diffraction Systems,* The Rigaku Journal **19**, 4 (2002).

[110] A. N. Broers, *Some experimental and estimated characteristics of the lanthanum hexaboride rod cathode electron gun*, J. Phys. E: Sci. Instrum. **2** 273 (1969).

[111] P. R. Davis, L. W. Swanson, J. J. Hutta and D. L. Jones, *Fabrication and characterization of rare earth hexaboride single-crystal materials*, Journal of Materials Science **21**, 825 (1986).

[112] G. D. Danilatos, *Environmental scanning electron microscopy and microanalysis*, Microchimica Acta **114**, 143 (1994).

[113] MicroMax™-007 HF, Rigaku,, more information available online at http://www.rigaku.com/generators/micromax007.html.

[114] P. Schardt, J. Deuringer, J. Freudenberger, E. Hell, W. Knüpfer, D. Mattern, and M. Schild., *New X-Ray Tube Performance in Computed Tomography by Introducing the Rotating Envelope Tube Technology*, Medical Physics **31**, 2699 (2004).

[115] R. W. Boyd, *Radiometry and the Detection of Optical Radiation* (John Wiley & Sons, New York, 1983), Chapter 2.4 – Lambertian Sources, pp. 20-22.

[116] A. Yoshioka, Y. Yamaguchi, K. Tamura and R. Shimizu, *Monte-Carlo Simulation of Spatial Distribution of Characteristic X-Rays in Multi-Film Targets: Source Size of Al Kα X-Rays in W/Al film targets*, Surf. Interface Anal. **36**, 1417 (2004).

[117] A. Yoshioka, Y. Yamaguchi, K. Tamura and R. Shimizu, *Monte-Carlo Simulation of Spatial Distribution of Characteristic X-Rays in Multi-Film Targets:. II: Spatial distribution of Continuous X-Rays and Temperature Elevation in W/Al film targets*, Surf. Interface Anal. **37**, 356 (2005).

[118] Y. Yamaguchi and R. Shimizu, *Monte-Carlo Simulation of Spatial Distribution of Characteristic X-Rays in Multi-Film Targets:. III: Optimum Design as applied to W/Al-Film Targets***,** Surf. Interface Anal. **39**, 343 (2007).

[119] J. Beutel, H. L. Kundel, and R. L. Van Metter, eds., Handbook of Medical Imaging – Volume 1. Physics and Psychophysics (SPIE Press, Washington, 2000), Fig. 1.8, p. 12.

[120] Photonic Science VHR, information available at http://www.photonic-science.co.uk/PDF/XDI-VHR.pdf.

[121] XR-100T-CZT, information available at www.amptek.com.

[122] B. A. Arnold, B. E. Bjarngard, and J. C. Klopping, *A modified pinhole camera method for investigation of X-ray tube focal spots*, Physics in Medicine and Biology **18** (4), 540-549 (1973).

[123] G. Lubberts and K. Rossmann, *Modulation Transfer Function Associated with Geometrical Unsharpness in Medical Radiography*, Physics in Medicine and Biology **12** (1), 65-77 (1967).

[124] S. Ehsan, J. Flynn Michael, and A. Reimann David, *A method for measuring the presampled MTF of digital radiographic systems using an edge test device*, Medical Physics **25** (1), 102-113 (1998).

[125] S. M. Hames, S. M. Hames, M. J. Flynn et al., *Measurement of very small (1-10 micron) X-ray focal spot intensity distributions*, Conference Record of the 1992 IEEE, (1992).

[126] T. Weitkamp, Chapter 5.3 – Microimaging and Tomography Instrument, pp 50.-65 in [180].

[127] X-Ray Test Pattern model 07-555, info available online at http:/www.gotopeo.com/doc/ cardinal_medical_imaging /DI1.pdf. (11 May 2008)

[128] J. Reinspach, Contact Lithography for X-ray Optics, Msc. Thesis, Royal Institute of Technology, Stockholm (2007).

[129] F. Salvat, J. M. Fernández-Varea and J. Sempau, PENELOPE-2006 A Code System for Monte Carlo Simulation of Electron and Photon Transport, OECD, Nuclear Energy Agency, Issy-les-Moulineaux, France, (2006). http://www.nea.fr/html/dbprog/peneloperef.html (11 May 2008)

[130] X. Llovet, J. M. Fernández-Varea J. Sempau and F. Salvat, *Monte Carlo simulation of X-ray emission using the general-purpose code PENELOPE*, Surface and Interface Analysis **37** (11), 1054 (2005).

[131] R. Gauvin, P. Hovongton, D. Drouin, P. Horny, H. Demers, and A. R. Couture, CASINO - Monte Carlo Simulation of Electron Trajectory in Solids, available online at http://www.gel.usherb.ca/casino. (11 May 2008)

[132] P. Hovington, D. Drouin and R. Gauvin *CASINO: A new Monte Carlo Code in C Language for Electron Beam Interaction - part I: Description of the Program*, Scanning **19**, 1 (1997).

[133] D. Drouin, P. Hovington and R. Gauvin *CASINO: A new Monte Carlo Code in C Language for Electron Beam Interaction - part II: Tabulated Values of the Mott Cross Section*, Scanning **19**, 20 (1997).

[134] P. Hovington, D. Drouin, R. Gauvin, D. C. Joy, N. Evans *CASINO: A new Monte Carlo Code in C Language for Electron Beam Interaction - part III: Stopping Power at Low Energies*, Scanning **19**, 29 (1997).

[135] D. Drouin, A. Réal Couture, D. Joly, X. Tastet, V. Aimez and R. Gauvin *CASINO V2.42 - A Fast and Easy-to-use Modeling Tool for Scanning Electron Microscopy and Microanalysis Users***,** Scanning **29**, 92 (2007).

[136] N. W. M. Ritchie, NISTMonte - Monte Carlo Simulation of Electron and X-Ray Transport in Solid Materials, available online at http://www.cstl.nist.gov/div837/837.02/epq/index.html. (11 May 2008)

[137] J. Valjakka, J. Utriainen, T. Åberg and J. Tulkki, *Direction-dependent initial-state relaxation in oxygen K x-ray emission*, Phys. Rev. B **32**, 6892 (1985).

[138] P. A. C. Jansson, U. Vogt and H. M. Hertz, *Liquid-nitrogen-jet laser-plasma source for compact soft x-ray microscopy*, Rev. Sci. Instrum. **76**, 043503 (2005).

[139] B. Buijsse, *keV-Electron-Based Table-Top Soft X-Ray Source*, Proc. SPIE. **4502**, 74 (2001).

[140] J. F Adam, J. P Moy, and J.S usini, *Table-Top Water Window Transmission X-Ray Microscopy: Review of the Key Issues, and Conceptual Design of an Instrument for Biology*, Rev. Sci. Instrum. **76**, 091301 (2005).

[141] M. Schlie, *Monte Carlo Simulations of Liquid-Jet-Anode Soft and Hard X-Ray Sources*, Msc. Thesis, Royal Institute of Technology, Stockholm (2007).

[142] Spellman XLF Series 600W, information available online at http://spellmanhv.com/pdf/XLF.pdf (May 2008).

[143] G. F. Rempfer, *Methods of calculating resolution in electron microscopy: Scherzer's equation, circles of least confusion and the intensity distribution approach.*, Ultramicroscopy, **47**, 241 (1992)

[144] G. Webster, R. Hilgenfeld, *Perspectives on Single Molecule Diffraction Using the X-Ray Free Electron Laser*, Single Molecules **3**, 63 (2002).

[145] T. Weitkamp, *Absorption and phase-contrast imaging in 2D and 3D*, Tutorial lecture notes, XTOP 2006, available online at http://xtop2006.fzk.de/tutorials-public/weitkamp1.pdf (May 15 2008)

[146] E. Krestel, ed., Imaging Systems for Medical Diagnostics (Siemens Aktiengesellschaft, Berlin and Munich, 1990), 2nd ed., Chapter 7.1.2.2 – Dependence of the Percentage of Scattered Radiation on the Beam Parameters, pp. 249-250.

[147] E. Krestel, ed., Imaging Systems for Medical Diagnostics (Siemens Aktiengesellschaft, Berlin and Munich, 1990), 2nd ed., Chapter 7.1.2.3 – 7.1.2.5, pp. 250-254.

[148] P. A. C Takman, H. Stollberg, G. A. Johansson, A. Holmberg, M. Lindblom and H. M. Hertz, *High-resolution compact X-ray microscopy*, J. Micr. **226,** 175 (2007).

[149] W. Chao, B. D. Harteneck, J. A. Liddle, E. H. Anderson and D. T. Attwood, *Soft X-ray microscopy at a spatial resolution better than 15 nm,* Nature **435**, 1210 (2005).

[150] V. E. Cosslett, W. C. Nixon, *X-ray Shadow Microscopy*, Nature **170**, 436 (1952)

[151] W. C. Nixon, *High-Resolution X-Ray Projection Microscopy*, Proc. R. Soc. **232**, 475 (1955)

[152] H. R.F Horn and H. G Waltinger, *How to Obtain and use X-Ray Projection Microscopy in the SEM*, Scanning **1**, 100 (1978).

[153] A. Sasov and D. Van Dyck, *Desktop X-Ray Microscopy and Microtomography*, J. Microsc. **191**, 151 (1998).

[154] S. C. Mayo, P. R. Miller, S. W. Wilkins, T. J. Davis, D. Gao, T. E. Gureyev, D. Paganin, D. J. Parry, A. Pogany, and A. W. Stevenson, *Quantitative X-Ray Projection Microscopy: Phase-Contrast and Multi-Spectral Imaging*, J. Micr. **207**, 79 (2002).

[155] D. Gao, S. Wilkins, D. Parry, T. Gureyev, P. Miller, and E. Hanssen, *X-ray ultramicroscopy using integrated sample cells*, Opt. Express **14**, 7889 (2006).

[156] S. W. Wilkins, P. R. Miller, "X-Ray Micro-Target Source", US Patent 7,050,540 (2006).

[157] S. C. Mayo, P. R. Miller, J. Sheffield-Parker, T. Gureyev and S. W. Wilkins, *Attainment of <60nm Resolution in Phase-Contrast X-ray Microscopy using an add-on to an SEM,* Proc. 8th Int. Conf. X-ray Microscopy IPAP Conf. Series 7, pp. 343-345.

[158] F. Arfelli *et al.*, *Mammography with Synchrotron Radiation: Phase-DetectionTechniques*, Radiology **215**, 286 (2000).

[159] E. D. Pisano, *Human Breast Cancer Specimens: Diffraction-Enhanced Imaging with Histologic Correlation-Improved Conspicuity of Lesion Detail Compared with Digital Radiography*, Radiology **214**, 895 (2000).

[160] J. Mollenhauer, M. E. Aurich, Z. Zhong, C. Muehleman, A. A. Cole, M. Hasnah, O. Oltulu, K. E. Kuettner, A. Margulis, and L. D. Chapman, *Diffraction-Enhanced XRay Imaging of Articular Cartilage*, J. Osteoarthritis and Cartilage **10**, 163 (2002).

[161] M. Z. Kiss, D. E. Sayers, Z. Zhong, C. Parham, and E. D. Pisano, *Improved Image Contrast of Calcifications in Breast Tissue Specimens Using Diffraction Enhanced Imaging*, Phys. Med. Biol. **49**, 3427 (2004).

[162] A. Momose, *Phase-Sensitive Imaging and Phase Tomography Using X-Ray Interferometers*, Opt. Express **11**, 2303 (2003).

[163] R. Fitzgerald, *Phase-Sensitive X-Ray Imaging*, Phys. Today **53**, 23 (2000).

[164] R. A. Lewis *et al.*, *Diffraction-Enhanced Imaging: Improved Contrast and Lower Dose X-Ray Imaging*, Proc. SPIE **4682**, 286-297 (2002).

[165] S. W. Wilkins, T. E. Gureyev, S. C. Mayo, Y. I. Nesterets, D. M. Paganin, A. Pogany, A. W. Stevenson, *Hard X-ray phase-contrast imaging for medical applications - physicist's dream or radiologist's mainstream*, 2nd International Symposium on Portable Synchrotron Light Sources and Advanced Applications. AIP Conference Proceedings, **902**, 33, (2007).

[166] V. N. Ingal, E. A. Beliaevskaya, A. P. Brianskaya, and R. D. Merkurieva, *Phase Mammography – A New Technique for Breast Investigation*, Phys. Med. Biol. **43**, 2555 (1998).

[167] D. J. Vine, D. M. Paganin, K. M. Pavlov et al., *Analyzer-based phase contrast imaging and phase retrieval using a rotating anode x-ray source,* Appl. Phys. Letters **91** (25), 254110 (2007).

[168] F. Pfeiffer, T. Weitkamp, O. Bunk and C. David, *Phase retrieval and differential phase-contrast imaging with low-brilliance X-ray sources*, Nature Physics, **2**, 258 (2006).

[169] M. Engelhardt, J. Baumann, M. Schuster, C. Kottler, F. Pfeiffer, O. Bunk, and C. David, *High-resolution differential phase contrast imaging using a magnifying projection geometry with a microfocus x-ray source*, Appl. Phys. Lett. **90**, 224101 (2007).

[170] J. W. Goodman, Chapter 4.5.2 –Fresnel Diffraction by a Sinusoidal Amplitude Grating – Talbot Images, pp 87-89 in [179].

[171] A. Snigirev, I. Snigireva, V. Kohn, S. Kuznetsov, and I. Schelokov, *On the possibilities of x-ray phase contrast microimaging by coherent high-energy synchrotron radiation*, Rev. Sci. Instrum. **66**, 5486 (1995).

[172] P. Cloetens, R. Barrett, J. Baruchel, J. P. Guigay, *Phase objects in synchrotron radiation hard x-ray imaging,* J. Phys. D: Appl. Phys. **29,** 133 (1996).

[173] S. W. Wilkins, T. E. Gureyev, D. Gao, A. Pogany, and A. W. Stevenson, *Phase-Contrast Imaging Using Polychromatic Hard X-Rays*, Nature **384**, 335 (1996).

[174] X. Wu and H. Liu, *Clinical Implementation of X-Ray Phase-Contrast Imaging:Theoretical Foundations and Design Considerations*, Med. Phys. **30**, 2169 (2003).

[175] K. A. Nugent, T. E. Gureyev, D. F. Cookson et al., *Quantitative Phase Imaging Using Hard X Rays,* Physical Review Letters **77**, 2961 (1996).

[176] P. Cloetens, W. Ludwig, J. Baruchel, D. Dyck, J. Landuyt, J. P. Guigay, and M. Schlenker, *Holotomography: Quantitative phase tomography with micrometer resolution using hard synchrotron radiation x rays*, Appl. Phys. lett. **75**, 2912 (1999).

[177] D. Paganin, S. C. Mayo, T. E. Gureyev et al., *Simultaneous phase and amplitude extraction from a single defocused image of a homogeneous object*, Journal of Microscopy **206**, 33 (2002).

[178] F. Pfeiffer, O. Bunk, C. Kottler, C. David, *Tomographic reconstruction of three-dimensional objects from hard X-ray differential phase contrast projection images*, Nucl. Instr. and Meth. **580**, 925 (2007).

[179] J. W. Goodman, *Introduction to Fourier Optics*, second edition, (McGraw-Hill 1996).

[180] T. Weitkamp, *Imaging and Tomography with High Resolution Using Coherent Hard Synchrotron Radiation*, Ph.D. Thesis, Hamburg University (2002).

[181] D. Attwood, Chapter 8.6 – The Van Cittert-Zernike Theorem, pp 321-330 in [189].

[182] A. Pogany, D. Gao, and S. W. Wilkins, *Contrast and resolution in imaging with a microfocus x-ray source*, Rev. Sci. Instr. 68, 2774 1997).

[183] J. W. Goodman, Chapter 6.1.3 – Polychromatic Illumination: The Coherent and Incoherent Cases, pp 130-134 in [179].

[184] D. Attwood, Chapter 8 – Coherence at Short Wavelengths, pp 301-336 in [189].

[185] D. Attwood, Chapter 9.2 – The Fresnel Zone Plate Lens, pp 342-366 in [189].

[186] J. W. Goodman, Chapter 4.2 – The Fresnel Approximation, pp 67-73 in [179].

[187] T. Weitkamp, Chapter 2.3 – Propagation in Free Space, pp. 19-21, in [180].

[188] J. M. Cowley, Diffraction Physics, (Elsevier, North-Holland, Amsterdam, 1995)

[189] D. Attwood, Soft X-Rays and Extreme Ultraviolet Radiation (Cambridge University Press, New York, 1999).

[190 J. Als-Nielsen, D. McMrrow, Elements of Modern X-Ray Physics (Wiley , New York, 2001).

[191] B. K. Agarwal, X-Ray Spectroscopy, vol. 15 of Springer Series in Optical Sciences (Springer-Verlag, Berlin, 1991), 2nd ed.

[192] A. G. Michette, and C. J. Buckley, ed., X-Ray Science and Technology (Institute of Physics Publishing, Bristol, 1993).

[193] A. H. Compton, and S. K. Allison, X-Rays in Theory and Experiment (Macmillan and Company, London, 1935), 2nd ed.

[194] H. Haken, and H. C. Wolf, The Physics of Atoms and Quanta (Springer-Verlag, Berlin, 1996), 5th ed.

[195] J. Orloff, Chapter 9 – The Scanning Electron Microscope, pp 361-400, in [20].

[196] J. I. Goldstein, and H. Yakowitz, eds., Practical Scanning Electron Microscopy (PlenumPress, New York, 1975), Figs. 3.4 and 3.7b, pp. 58 and 62.

[197] Electron Microprobe Techniques Class Notes, Northern Arizona University. Available online at http://www4.nau.edu/microanalysis/microprobe/Interact-Effects.html.

[198] M. Green and V. E. Cosslett, *Measurements of K, L and M Shell X-ray Production Efficiencies,* J. Phys. D: Appl. Phys. **1**, 425 (1968).

[199] X-Ray Interactions with Matter, Center for X-Ray Optics. Available online at http://henke.lbl.gov/optical_constants/ (15 May 2008).

[200] M. J. Berger, J. H. Hubbell, S. M. Seltzer, J. Chang, J. S. Coursey, R. Sukumar, and D. S. Zucker, *XCOM: Photon Cross Sections Database*, ver. 3.1, available online at http://physics.nist.gov/PhysRefData/Xcom/Text/XCOM.html, 1 May 2008.